



Simultaneous temporal and spectral analysis of noise-like pulses in a mode-locked figure-eight fiber laser

O. S. TORRES-MUÑOZ,^{1,*} O. POTTIEZ,¹ Y. BRACAMONTES-RODRIGUEZ,¹
J. P. LAUTERIO-CRUZ,² H. E. IBARRA-VILLALON,¹ J. C. HERNANDEZ-
GARCIA,^{2,3} M. BELLO-JIMENEZ,⁴ AND E. A. KUZIN⁵

¹Centro de Investigaciones en Óptica (CIO), Loma del Bosque 115, Col. Lomas del Campestre, León, Gto. 37150, México

²Departamento de Electrónica, División de Ingenierías CIS, Universidad de Guanajuato, Carretera Salamanca-Valle de Santiago Km 3.5 + 1.8 Km, Comunidad de Palo Blanco, Salamanca, Gto. 36885, México

³Consejo Nacional de Ciencia y Tecnología, Av. Insurgentes Sur No. 1582, Col. Crédito Constructor, Del. Benito Juárez, C.P. 039040, México

⁴Instituto de Investigación en Comunicación Óptica, Universidad Autónoma de San Luis Potosí, Av. Karakorum 1470, Lomas 4ta Secc., San Luis Potosí, S.L.P. 78210, México

⁵Instituto Nacional de Astrofísica, Óptica y Electrónica (INAOE), L. E. Erro 1, Sta. Ma. Tonantzintla, Pue. 72824, México

*osccar_saltomu@live.com

Abstract: We present an experimental study of complex noise-like pulse dynamics in a passively mode-locked figure-eight fiber laser, by performing simultaneous temporal and spectral mapping of the waveform sequences. The simultaneous measurements allow us to relate temporal and spectral events. We found in particular that the evolution of energy and of temporal features such as the number and width of the wave packets is correlated to spectral variations, namely of the central wavelength and bandwidth of the instantaneous spectrum. The simultaneous temporal and spectral measurements also allowed a substantial improvement in the precision of the latter, which was performed using the dispersive Fourier transform method. In particular, this enhanced precision allowed measuring the subtle spectral differences between the two laser outputs and tracking their evolution over the cycles, providing crucial information that allowed to determine the physical phenomena involved in the observed dynamics.

© 2019 Optical Society of America under the terms of the [OSA Open Access Publishing Agreement](#)

1. Introduction

It has been observed that passively mode-locked fiber lasers can operate in a wide variety of regimes, such as conservative solitons [1,2], similaritons [3–5] and dissipative solitons [6,7], etc. The regimes mentioned above correspond to stationary or close to stationary regimes; however, operating a fiber laser far from a steady state, we can also find the so-called noise-like pulses (NLPs) [8–33]. NLPs are long (~ns) bunches of optical radiation with a fine inner structure (sub-ps) that present a complex and chaotic behavior, with constantly and randomly varying time duration and amplitude. The statistical study of this type of dynamics has come to reveal extreme fluctuations, which under some conditions result in rare events like optical rogue waves [34–38]. The first studies on NLPs were published in the 90s [8]. Due to the extremely complex nature and variability of NLPs, their characterization is very challenging, and until now there is no solid understanding of their formation mechanisms and their behavior, even though several theoretical and experimental works have been carried out for this purpose [8–10,13,16]. The complexity and the chaotic variations of the fine inner structure (at sub-ps scale) of NLPs justify their classification among the non-stationary



Single and dual-wavelength noise-like pulses with different shapes in a double-clad Er/Yb fiber laser

E. BRAVO-HUERTA,¹ M. DURÁN-SÁNCHEZ,^{1,2,*} R. I. ÁLVAREZ-TAMAYO,³ H. SANTIAGO-HERNÁNDEZ,⁴ M. BELLO-JIMÉNEZ,⁵ B. POSADA-RAMÍREZ,¹ B. IBARRA-ESCAMILLA,¹ O. POTTIEZ,⁶ AND E. A. KUZIN¹

¹Instituto Nacional de Astrofísica, Óptica y Electrónica (INAOE), L. E. Erro 1, Sta. Ma. Tonantzintla, Puebla, 72824, México

²CONACYT-Instituto Nacional de Astrofísica, Óptica y Electrónica, A. P. 51 y 216, CP 72000, Puebla, México

³CONACYT—Universidad Autónoma de Nuevo León, Av. Universidad S/N, San Nicolás de los Garza, Nuevo León 66451, México

⁴Universidad de Guadalajara, Departamento de Electrónica, Av. Revolución 1500, Guadalajara, Jalisco 44840, México

⁵Instituto de Investigación en Comunicación Óptica, Universidad Autónoma de San Luis Potosí, Av. Karakorum, San Luis Potosí, 78210, México

⁶Centro de Investigaciones en Óptica (CIO), Loma del Bosque 115, Col. Lomas del Campestre, León, Guanajuato 37150, México

*manueld@inaoep.mx

Abstract: We report an experimental study of passive harmonic mode-locking in an all-fiber switchable dual-wavelength Er/Yb double-clad laser. The proposed scheme supports single- and dual-wavelength operation of mode-locked pulses with rectangular, h-like and trapezoidal shapes in a noise-like pulse regime. Single-wavelength emissions at $\lambda_1 = 1545.1$ and $\lambda_2 = 1563.6$ nm were obtained for pump power values of 9.42 and 6.31 W, achieving pulse durations of up to 18 and 11.8 ns, respectively. At an intermediary pump power of 7.5 W, dual-wavelength emission is obtained and pulses of around 3.59 ns are generated. Additionally, the transition dynamics until 4th-order harmonic mode-locking is also observed. Different laser operation regimes of fundamental and different orders of harmonic mode-locking, with rectangular, h-shaped or trapezoidal shaped pulses are obtained with the same laser configuration with simple and well-defined plates and pump power adjustments.

© 2019 Optical Society of America under the terms of the [OSA Open Access Publishing Agreement](#)

1. Introduction

The operation characteristics of a passively mode-locked fiber laser (PMLFL) allows the generation of coherent and stable waveforms, including conventional and dispersion-managed solitons [1], and a variety of dissipative solitons [2]. Moreover, quasi-stable patterns of solitons involved in dynamics such as soliton rain [3] and noise-like pulses (NLPs) [4] were also demonstrated, even in symbiotic or multiple-soliton (MS) regimes depending of their packet-forming mechanism or their coherence nature [5]. Due to their stability, compactness and ease of use, nowadays PMLFLs have become fundamental devices in optics and materials laboratories around the world. However, the limited average output power originated from the low gain provided by single-mode active fibers is a challenge to overcome [6]. In this sense, rare-earth-doped double-clad fibers used as gain media has proved to be a reliable option to significantly increase the gain factor and efficiency of single-mode fiber lasers operation by using cladding pumping from high-power multimode sources [7].

In recent years, different laser regimes from harmonic generation [8,9] to the formation of different soliton patterns [10] passing by dissipative soliton resonance (DSR) [11–13], or

Real-time temporal-spectral analysis of complex dynamics involving multiple soliton states in a dual-wavelength passively mode-locked fiber ring laser

O S Torres-Muñoz¹, O Pottiez¹, Y E Bracamontes-Rodríguez¹,
J P Lauterio-Cruz², J C Hernandez-García^{2,3}, M Bello-Jimenez⁴
and E A Kuzin⁵

¹ Centro de Investigaciones en Óptica (CIO), Loma del Bosque 115, Col. Lomas del Campestre, León, Gto. 37150, Mexico

² Departamento de Electrónica, División de Ingenierías CIS, Universidad de Guanajuato, Carretera Salamanca-Valle de Santiago Km 3.5 + 1.8 Km, Comunidad de Palo Blanco, Salamanca, Gto. 36885, Mexico

³ Consejo Nacional de Ciencia y Tecnología, Av. Insurgentes Sur No. 1582, Col. Crédito Constructor, Del. Benito Juárez, C.P. 039040, Mexico

⁴ Instituto de Investigación en Comunicación Óptica, Universidad Autónoma de San Luis Potosí, Av. Karakorum 1470, Lomas 4ta Secc., San Luis Potosí, S.L.P. 78210, Mexico

⁵ Instituto Nacional de Astrofísica, Óptica y Electrónica (INAOE), L. E. Erro 1, Sta. Ma. Tonantzintla, Pue. 72824, Mexico

E-mail: osccar_saltomu@live.com

Received 25 June 2019

Accepted for publication 9 September 2019

Published 25 September 2019



Abstract

We present an experimental study of complex dissipative solitons dynamics in a passively mode-locked fiber ring laser. Recently, thanks to real-time spectroscopy techniques such as the dispersive Fourier transform (DFT), it has been possible to study the complex internal dynamics of soliton molecules. However, most of the works have been limited to the study of intermolecular or intramolecular dynamics involving a small number of solitons within a single compact soliton packet, to which the DFT technique applies naturally. In this work, we study the dynamics of complex arrangements of multiple solitons, extending the analysis to regimes where multiple soliton packets at different wavelengths coexist and interact in the cavity, probing simultaneously the internal dynamics of various short-lived soliton molecules, as well as the collective dynamics of the different soliton packets distributed in the cavity, all of which is made possible by simultaneous analysis in the temporal and spectral domains. This allows to relate temporal dynamics at different time scales, as well as temporal and spectral events. In particular, we report the experimental observation of the dynamics of the Kelly sidebands that flank the soliton spectra, and relate it to temporal and spectral events such as extinctions of soliton packets with pulsating amplitude, spectral narrowing, and with energy fluctuations.

Keywords: dissipative solitons, Kelly sidebands, soliton molecules, mode-locked fibre laser

(Some figures may appear in colour only in the online journal)

Unrestricted wreath products and sofic groups

Goulmara Arzhantseva

*Faculty of Mathematics, University of Vienna
Oskar-Morgenstern-Platz 1, Vienna 1090, Austria
goulmara.arzhantseva@univie.ac.at*

Federico Berlai

*Department of Mathematics
University of the Basque Country UPV/EHU
Barrio Sarriena s/n Leioa 48940, Spain
federico.berlai@ehu.eus*

Martin Finn-Sell

*Faculty of Mathematics, University of Vienna
Oskar-Morgenstern-Platz 1, Vienna 1090, Austria
martin.finn-sell@univie.ac.at*

Lev Glebsky

*Research Institute of Optical Communication
Autonomous University of San Luis Potosí
Av. Karakorum 1470, Lomas 4a
San Luis Potosí 78210, Mexico
glebsky@cactus.iico.uaslp.mx*

Received 30 April 2018

Accepted 9 October 2018

Published 15 November 2018

Communicated by A. Ol'shanskii

We show that the unrestricted wreath product of a sofic group by an amenable group is sofic. We use this result to present an alternative proof of the known fact that any group extension with sofic kernel and amenable quotient is again a sofic group. Our approach exploits the famous Kaloujnine–Krasner theorem and extends, with an additional argument, to hyperlinear-by-amenable groups.

Keywords: Wreath products; amenable; sofic; hyperlinear groups.

Mathematics Subject Classification 2010: 20F65, 03C25



TRUE SPECTRUM OF A FINITE FOURIER TRANSFORM

Javier Diaz-Vargas¹, Lev Glebsky² and Carlos Jacob Rubio-Barrios¹

¹Universidad Autónoma de Yucatán

Mexico

e-mail: javier.diaz@correo.uady.mx

carlos.rubio@correo.uady.mx

²Universidad Autónoma de San Luis Potosí

Mexico

e-mail: glebsky@cactus.iico.uaslp.mx

Abstract

In this paper, we deal with a finite abelian group G and the abstract Fourier transform $\mathcal{F} : \mathbb{C}^G \rightarrow \mathbb{C}^{\hat{G}}$. Then we consider $\tilde{j} \circ \mathcal{F} : \mathbb{C}^G \rightarrow \mathbb{C}^{\hat{G}}$, where $\tilde{j} : \mathbb{C}^{\hat{G}} \rightarrow \mathbb{C}^G$ is defined by the composition with a bijection $j : G \rightarrow \hat{G}$. (\tilde{j} is a pullback of j .) In particular, we show that $(\tilde{j} \circ \mathcal{F})^2$ is a permutation if and only if j is a group isomorphism. Then we study how the spectrum of $\tilde{j} \circ \mathcal{F}$ depends on the isomorphism j .

Received: August 21, 2019; Accepted: September 24, 2019

2010 Mathematics Subject Classification: Primary 11T06; Secondary 13M10.

Keywords and phrases: finite abelian group, character, Fourier transform, Gauss sum, orthogonality relations, Fourier inversion.



Effects of Mg incorporation in cubic GaN films grown by PAMBE near Ga rich conditions



V.D. Compeán-García^a, H. Moreno-García^b, E. López-Luna^b, H. Pérez Ladrón de Guevara^c,
A. Escobosa Echavarría^d, Y. Kudriavtsev^d, F.J. Rodríguez-Aranda^b, A.G. Rodríguez^b, M.A. Vidal^{b,*}

^a CONACyT-Coordinación para la Innovación y Aplicación de la Ciencia y Tecnología (CIACyT), Universidad Autónoma de San Luis Potosí (UASLP), Álvaro Obregón 64, San Luis Potosí 78000, Mexico

^b Coordinación para la Innovación y Aplicación de la Ciencia y Tecnología (CIACyT), Universidad Autónoma de San Luis Potosí (UASLP), Álvaro Obregón 64, San Luis Potosí 78000, Mexico

^c Centro Universitario de los Lagos, Universidad de Guadalajara, Av. Enrique Díaz de León 1144, col. Paseos de la Montaña, Lagos de Moreno, Jalisco 47460, Mexico

^d Electric Engineering Department, Centro de Investigación y Estudios Avanzados del IPN, Apartado Postal 14-740, 07000 México D.F., Mexico

ARTICLE INFO

Keywords:

Cubic GaN diode
Mg p-type doping
Plasma-assisted molecular beam epitaxy

ABSTRACT

The structural and electrical properties of Mg-doped cubic GaN epi-layers grown by plasma-assisted molecular beam epitaxy (PAMBE) near Ga rich conditions are investigated. The diffraction of high-energy reflected electrons (RHEED) in situ, in addition to structural studies of X-ray diffraction, show that the fraction of hexagonal and crystal twinning inclusions decreases when the Mg flux increases. The condition for the higher incorporation of Mg where the electrical properties are optimized is highly sensitive to the flow ratio Mg/Ga. The p-doping level steadily increases with increasing Mg flux. The Mg concentration obtained by secondary ion mass spectroscopy (SIMS) from samples grown at Mg temperatures from 200 °C to 700 °C are in a range between 2×10^{19} to 2×10^{20} atoms/cm³. The highest mobility and p-type doping level achieved, determined from Hall measurements, were 28.2 cm²/V-s and 2×10^{19} cm⁻³, respectively. We corroborate that the Mg doped c-GaN films are suitable for the construction of optoelectronic devices based on cubic III-Nitrides.

1. Introduction

Cubic gallium nitride (c-GaN) has a bandgap of 200 meV lower than the hexagonal phase (h-GaN) [1], for this reason, it is possible to modulate to the visible region with less amount of indium in the zinc-blend than wurtzite InGaN alloy [2–5]. In addition, due to higher crystalline symmetry, resulting in more isotropic properties and no spontaneous polarization induced-electric fields in the direction parallel to the c-axis, it is possible to grow the cubic InGaN alloy with a bandgap in the green region [2–9]. Consequently, this alloy is attractive for applications in photovoltaic and optoelectronic devices, including multiband solar cells, hydrogen production photoelectrodes, laser and light emitting diodes [10].

However, the development of optoelectronic, photovoltaic and electronic devices based on c-InGaN requires an efficient p-type doping and high-quality crystal structure. To our knowledge, limited reports of cubic III-Nitrides devices have been found in the literature [11,12], this is in part for the inefficient p-type doping or the main disadvantage in the synthesis of c-GaN, the lack of native substrates and a low-quality

crystalline film due to the hexagonal inclusions [13,14]. Therefore, improvements in the efficiency of p-type doping of the c-GaN epilayers are essential for enhanced manufacturing technology of cubic III-Nitrides semiconductors.

This paper presents a study of the influence of the Mg flux on the electrical and structural properties of Mg doping c-GaN, grown by molecular beam epitaxy on MgO (100) substrates, near to the regimen of Ga rich conditions. This study is performed by varying the Mg flux (with magnesium effusion cell temperature in a range from 200 to 700 °C) with growth conditions of c-GaN films at 720 °C.

2. Experimental

Epitaxial growth of Mg-doped c-GaN films heterostructures under study was performed on 1 cm² MgO(001) substrates by a vertical PAMBE with standard effusion cells for Ga, Mg, and an high-purity N₂ RF plasma cell [2,6]. The purity of Ga and Mg sources are 99.9995%.

Prior to the growth of the Mg-doped GaN epi-layer, the substrate was cleaned on a 10 min trichloroethylene and acetone ultrasonic bath.

* Corresponding author.

E-mail address: miguel.vidal@uaslp.mx (M.A. Vidal).

<https://doi.org/10.1016/j.mssp.2018.12.019>

Received 8 November 2018; Received in revised form 17 December 2018; Accepted 19 December 2018

1369-8001/ © 2018 Published by Elsevier Ltd.



PAPER

Hydrazine-free chemical bath deposition of WSe₂ thin films and bi-layers for photovoltaic applicationsRECEIVED
14 January 2019REVISED
26 February 2019ACCEPTED FOR PUBLICATION
12 March 2019PUBLISHED
23 August 2019

G A Guerrero , A G Rodríguez and H Moreno-García

Coordinación para la Innovación y la Aplicación de la Ciencia y la Tecnología (CIACYT), Universidad Autónoma de San Luis Potosí (UASLP), Álvaro Obregón 64, 78000 San Luis Potosí, S L P, México

E-mail: harumi.moreno@uaslp.mxKeywords: WSe₂, bilayer, chemical bath deposition, diode, hydrazine-free

Abstract

We report the photovoltaic performance of a diode based on a p-type tungsten diselenide (WSe₂) active region. The device is formed by WSe₂ and cadmium sulfide (CdS) layers, both obtained via chemical bath deposition. A novel hydrazine-free chemical formulation allows deposition of WSe₂ on glass and flexible Hastelloy substrates. Characterization of WSe₂ via Raman spectroscopy shows four bands at 189, 244, 293, and 588 cm⁻¹. The strongest band at 293 cm⁻¹ is assigned to the interlayer interaction mode of the WSe₂ layers. The photoluminescent characterization of Hastelloy/CdS/WSe₂ samples exhibits two excitonic transitions at 1.7860 and 1.7899 eV. The current density-voltage (J-V) measurements of the CdS/WSe₂ structure show a photovoltaic response with V_{OC} = 180 mV, J_{SC} = 0.07 mA cm⁻², and FF = 0.22.

1. Introduction

Ultra-thin transition metal dichalcogenides (TMD) such as tungsten disulfide (WS₂) and tungsten diselenide (WSe₂) have attracted wide interest due to the enhanced quantum confinement effects attainable in quasi-two-dimensional (2D) crystals. Because of the physics of the lamellar structure of TMD crystals, their optical band gap increases and shifts from indirect to direct as the number of stacked layers decreases [1–5]. The direct band gap (E_g) of WSe₂ varies from 1.36 eV at 11 monolayers to 1.65 eV in the 2D limit of a single monolayer (ML), according to theoretical studies and experimental values [4, 6]. Two-dimensional WSe₂ structures are usually obtained by the application of some type of exfoliation of the synthesized bulk material, for example modified liquid exfoliation [7], laser exfoliation [8, 9], mechanical exfoliation [5, 10, 11], or exfoliation employing a low molecular weight adenine-functionalized supramolecular polymer (A-PPG) [12]; however, they have also been obtained *in situ* by physical and chemical techniques such as spray casting deposition [13] hydrothermal synthesis [14, 15], atomic layer deposition (ALD) [16], sputtering [17], a combination of sputtering-selenization [18] and chemical vapor deposition (CVD) [19, 20], chemical vapor transport (CVT) [21], and chemical bath depositions (CBD) using hydrazine as a chemical reducing agent [22].

The physical properties of WSe₂ have wide applications in electrical and optoelectronic nanodevices such as sub-5-nm gate field effect transistors (FETs) [5, 9, 23], supercapacitors [21], light-emitting diodes [24], the evaluation of hydrogen-reaction evolution using reduced graphene oxide (rGO) in WSe₂/rGo hybrid structures [25], gate-controlled field emission current [23], dye-sensitized cells [18], heterostructures [26–28], and thin-film solar cells [19, 29]. In the development of dye-sensitized solar cells, values of open circuit voltage (V_{OC}) of 620 mV, current density in short circuit (J_{SC}) of 20.4 mA cm⁻², fill factor (FF) of 0.65, and power conversion efficiency (PEC) of 8.22% [18] have been reported using a WSe₂/W film as counter electrode. Although molybdenum diselenide (MoSe₂) and WS₂ have already been applied in solar cells [17, 30], the application of WSe₂ in diodes as a monolayer is limited due to the difficulty of growing a uniform monoatomic layer over large areas. Chen *et al* recently reported the elaboration of a WSe₂ p-n homojunction diode using CVD to grow monolayer crystalline WSe₂ sheets [29]. Their diode exhibited clear rectifying behavior, but the photovoltaic response was not studied.

Algoritmo esteganográfico basado en autómatas celulares y en la sustitución de los bits menos significativos

Uriel López, Humberto Dávila, Luis Zapata, Marco Ramírez

Universidad Autónoma de San Luis Potosí,
Coordinación Académica Región Altiplano Oeste, México
tulio.torres@uaslp.mx

Resumen. En esta investigación se presenta un nuevo algoritmo de esteganografía para imágenes, utilizando la sustitución de los bits menos significativo y la regla local 90 de autómatas celulares. Este algoritmo es capaz de cifrar y ocultar los píxeles de la imagen en un proceso combinado. El factor PSNR indica que no existe una distorsión severa en la imagen esteganográfica, lo que en esta área se interpreta como a menor distorsión de la imagen esteganográfica, mayor es la probabilidad de pasar desapercibida y que no sea analizada. Sin embargo, en caso de que la imagen oculta sea extraída, ésta se encuentra protegida por una clave secreta. Este algoritmo transforma la imagen secreta a una imagen cifrada con distribución uniforme y sin correlación. Este algoritmo esteganográfico puede ser una nueva opción para ocultar y proteger imágenes relacionando ambos procesos.

Palabras clave: esteganografía, autómatas celulares, PSNR.

Steganographic Algorithm Based on Cellular Automata and the Replacement of Less Significant Bits

Abstract. This research presents a new steganography algorithm for images, using the least significant bit replacement and local rule 90 of cellular automata. This algorithm is able to encrypt and hide the image pixels in a combined process. The PSNR factor indicates that there is no severe distortion in the steganographic image, which in this area is interpreted as the less distortion of the steganographic image, the greater the probability of going unnoticed and that it is not analyzed. However, if the hidden image is extracted, it is protected by a secret key. This algorithm transforms the secret image to an encrypted image with uniform distribution and no correlation. This steganographic algorithm can be a new option to hide and protect images by relating both processes.

Keywords: steganography, cellular automata, PSNR.

Image Encryption System Based on Cellular Automata and S-Box

Juan Contreras¹, Marco Ramírez¹, Jesús Aboytes²

¹ Coordinación Académica Región Altiplano Oeste-UASLP, Salinas, Mexico

² Instituto de Investigación en Comunicación Óptica, UASLP, San Luis Potosí, Mexico
juanjosetorres96@outlook.com, tulio.torres@uaslp.mx,
agustin.aboytes@upslp.edu.mx

Abstract. This investigation presents an image encryption system and its security analysis, it is based on cellular automata and a substitution box. The joint of these two techniques, allow to encrypt digital images with a high adjacent redundancy and pass different statistical and differential tests and cryptanalytic attacks. The synchronization phenomenon of cellular automata, is sensitive to initial conditions, therefore has been used in Pseudo Random Number Generators (PRNG) and cryptosystems. In this system, the synchronization phenomenon is used to change the coefficients of the pixels, but the process is not equal for each bit, thus the s-box is used to make the system robust and for compliance with the bit independence criterion among others.

Keywords: image encryption, cellular automata, S-box.

1 Introduction

Nowadays, we can perform many operations for internet, thus facilitating processes and optimizing times. But, this requires providing security to users, given that their data are exposed on the transmissions or at the storage location. One of the techniques used to protect information are cryptographic algorithms. This technique consists of making the information unintelligible, in such a way that it can only be recovered using the correct key.

Currently, image encryption is a very active field of research, due to the multiple areas where it is required, for example: in the pay-television service, medical imaging systems, videoconferences, military communications, video surveillance, among others. Although there are several conventional encryption algorithms, such as AES (Advanced Encryption Standard), DES (Data Encryption Standard) and IDEA (International Data Encryption Algorithm), they have often been impractical for image encryption, due to the intrinsic properties of these, such as large volumes, a strong adjacent correlation, a high redundancy, among others [1]. Therefore, the security problem extends because the algorithms for image encryption must provide perceptual security and cryptographic security.

This has encouraged the search and implementation of new schemes for image encryption, such as the large number of encryption systems with a chaotic approach [2, 3, 4]. That is why in this research the synchronization of cellular automata is combined

Differential reflectance contrast technique in near field limit: Application to graphene

Cite as: AIP Advances 9, 045309 (2019); <https://doi.org/10.1063/1.5092339>

Submitted: 10 February 2019 . Accepted: 29 March 2019 . Published Online: 10 April 2019

L. F. Lastras-Martínez , D. Medina-Escobedo, G. Flores-Rangel, R. E. Balderas-Navarro, O. Ruiz-Cigarrillo, R. Castro-García , M. del P. Morales-Morelos, J. Ortega-Gallegos, and M. Losurdo



View Online



Export Online



CrossMark

AVS Quantum Science

Co-published with AIP Publishing



Coming Soon!



Chemical modification of titanium dioxide nanoparticles with dicarboxylic acids to mediate the UV degradation in polyethylene films

D. L. Zapata-Tello¹ · V. Escobar-Barríos² · J. A. Gonzalez-Calderon³  · Elías Pérez⁴

Received: 6 July 2019 / Revised: 31 October 2019 / Accepted: 10 December 2019
© Springer-Verlag GmbH Germany, part of Springer Nature 2019

Abstract

This work deals with the study of the degradation of films made of low-density polyethylene (LDPE) by the incorporation of commercial titanium dioxide nanoparticles (TiO₂ Nps). These nanoparticles were functionalized with three types of dicarboxylic acid, which have different length chain (glutaric, pimelic and azelaic acids), to improve their compatibility with LDPE. Besides, the effect of the functionalized TiO₂ Nps concentration on the photodegradation, roughness, mechanical and thermal stability of the nanocomposites was evaluated. The obtained results show that the organic coating helps to passivate the photodegradation of LDPE; the longer carbon chain of the dicarboxylic acid, the higher active sites on filler/polymer interface, which inhibits photodegradation. Also, it was elucidated that calcium, from the functionalization, increased the thermal stability of the polymer nanocomposites when exposed to UV radiation. The thermal, physical (surface wear) and aesthetic (color) properties of polyethylene, with the functionalized nanoparticles, were less affected when exposed to the weather, where it is attributed to the UV photo-stabilization of the polymer. The resultant materials (LDPE with functionalized TiO₂ Nps) can be used in diverse applications such as films for greenhouse and other agricultural applications, outdoor appliances (furniture and decks, for example), among others.

Keywords Polymer nanocomposites · UV-stability · Dicarboxylic acids · Titanium dioxide · Polyethylene

✉ J. A. Gonzalez-Calderon
amir@ifisica.uaslp.mx

Extended author information available on the last page of the article

Many-electron effective potential in low-dimensional nanostructures: Towards understanding the Wigner crystallization

Reyna Méndez-Camacho,^{1,2,*} Esteban Cruz-Hernández,¹ and Ramón Castañeda-Priego^{2,†}

¹*Coordinación para la Innovación y Aplicación de la Ciencia y la Tecnología, Universidad Autónoma de San Luis Potosí, Sierra Leona 550, 78210 San Luis Potosí, México*

²*División de Ciencias e Ingenierías, Campus León, Universidad de Guanajuato, Loma del Bosque 103, 37150 León, México*



(Received 4 February 2019; revised manuscript received 5 July 2019; published 29 August 2019)

We present the derivation and application of an analytical effective potential that is able to describe, in a simple way, the interaction of many electrons confined in low-dimensional structures of realistic size. The effective potential takes into account the contribution of both the electron-electron interaction inside the nanostructure and the quantum confinement by a surrounding material. With this model, we explore the electronic distribution in quantum wells, wires, and dots in the full range from doped to high-doped concentrations. We also use this effective potential to explicitly determine the parameters that trigger the formation of the Wigner molecule in quantum wires. The comparison with experimental data reported in the literature shows the accuracy and reliability of this potential model.

DOI: [10.1103/PhysRevB.100.085438](https://doi.org/10.1103/PhysRevB.100.085438)

I. INTRODUCTION

The strong confinement of electrical carriers, photons, and/or phonons in nanostructures can trigger unique physical phenomena that make those structures very attractive experimental systems with great potential applications in nanotechnology [1,2]. Currently, by means of different growth techniques such as hydride vapor phase epitaxy, metal-organic chemical-vapor deposition, and molecular-beam epitaxy, high-quality nanostructures of a wide range of materials, geometries, and doping levels can be synthesized [3–5].

Among the most fundamental and interesting questions observed in nanostructures are those related to the collective effect of electron-electron (e - e) interactions and quantum confinement [6–14]. One remarkable example where the competition between many-body forces and spatial restrictions leads to interesting phenomena is the Wigner crystallization; under specific conditions electrons spontaneously form a self-organized lattice in quantum wires (QWRs) [15–19].

When many-body interactions are explicitly included in the modeling of nanostructures, usually, long computational times and complex mathematical calculations are required to deal with realistic electronic densities and the nanometric or even micrometric size of the structures [10,13,20–24]. For that reason, in spite of the fundamental importance of the interaction of many electrons in the collective phenomena, the contribution of this interaction to the formation of new structures, such as the Wigner crystal, has remained a relatively unexplored field.

Recently, we proposed a simple approach to deal with the problem of many electrons confined in semiconductor QWRs by numerically solving the Schrödinger equation of

two nonrelativistic electrons without spin, confined in square QWRs of infinite barriers and interacting effectively through a Yukawa-like potential [25]. In that work, the use of the Yukawa potential allowed us to study the interaction of a large number of electrons just by selecting a screening parameter κ [25]. However, one of the main limitations to its application is the fact that the confinement effects produced by the nanometric cross section of the QWRs are not explicitly included in the model.

In this contribution, we derive an analytical effective potential that is able to describe the e - e interaction, via a Yukawa-like potential, as well as the confinement in all three spatial dimensions. The reliability of this effective potential is investigated by its comparison with the Yukawa approach [25] and with experimental observations of the Wigner crystallization in QWRs reported elsewhere [13,14].

II. EFFECTIVE POTENTIAL: DERIVATION AND SOME FEATURES

A. Analytical derivation

For the derivation of the effective potential, a system of electrons confined to a square GaAs structure embedded in a matrix of $\text{Al}_x\text{Ga}_{1-x}\text{As}$ (see Fig. 1) was considered. In such a system, the two-electron Hamiltonian is given by [25]

$$H = -\frac{\hbar^2}{2m_e^*} \nabla_i^2 + V_{e-w} + V_Y(r_{12}), \quad (1)$$

where $i = 1, 2$ accounts for the two electrons, $\hbar \equiv h/2\pi$, h is the Planck constant, m_e^* is the effective electron mass, and V_{e-w} is the electron-wall potential in the x - y plane. The e - e interaction was considered to have the form of a Yukawa-like potential $V_Y(r_{12})$ [26]. This approach is similar to the well-known jellium model typically employed in solid-state physics, but with the difference that we consider two

*reyna.mendez@uaslp.mx

†ramoncp@fisica.ugto.mx

Two-dimensional electron gas in a metal/amorphous oxide interface with spin-orbit interactionJose Manuel Flores-Camacho,^{1,*} Jorge Puebla,^{2,†} Florent Auvray,^{2,3} Alfonso Lastras-Martínez,¹
Yoshichika Otani,^{2,3} and Raul Eduardo Balderas-Navarro¹¹*Instituto de Investigación en Comunicación Óptica, Universidad Autónoma de San Luis Potosí, Álvaro Obregón 64,
78000 San Luis Potosi, Mexico*²*Center for Emergent Matter Science, RIKEN, Wako, Saitama 351-0198, Japan*³*Institute for Solid State Physics, University of Tokyo, Kashiwa, Chiba 277-8581, Japan*

(Received 18 December 2018; revised manuscript received 23 February 2019; published 24 December 2019)

The formation of novel two-dimensional electron gas (2DEG) with high mobility in metal/amorphous interfaces has motivated an ongoing debate regarding the formation and novel characteristics of these 2DEGs. Here we report an optical study, based on infrared spectroscopic ellipsometry, of nonmagnetic metal and amorphous semiconducting oxide (Cu/Bi₂O₃) interfaces that confirms the formation of a 2DEG with spin orbit coupling (SOC). The 2DEG optical response was simulated with a uniaxial diagonal dielectric tensor within a subnanometer thin layer, where its x and z component line shapes resolved in both free-electron and peaklike contributions, resulting in very similar theoretical predictions [M. Xie *et al.*, *Phys. Rev. B* **89**, 245417 (2014)] of a 2DEG confined in the normal direction of a perovskite interface. In particular, the small but finite conducting character of the z component provides an unambiguous signature of the presence of the 2DEG in the Cu/Bi₂O₃ system. Although the original constituent materials do not possess SOC, the resulting interfacial hybridization of such states induce electronic asymmetric wave functions. This work demonstrates the detection of 2DEG in amorphous crystals, allowing one to study its challenging interfacial phenomena such as SOC and interface-bulk coupling, overcoming an experimental impediment which, for decades, has held back important advancements for the understanding of 2DEGs in amorphous materials.

DOI: [10.1103/PhysRevB.100.235449](https://doi.org/10.1103/PhysRevB.100.235449)**I. INTRODUCTION**

The concept of two-dimensional electron gas (2DEG) has contributed enormously to the understanding of the rich phenomena of electrons confined at surfaces and interfaces. In high-quality semiconductor heterostructures, 2DEG confinement-induced enhancement of electron mobility lead to technology advancements and scientific discoveries, such as the fractional Quantum Hall effect [1]. The continuous development of growth techniques nowadays allows us to obtain enough good quality heterostructures from oxides, forming 2DEGs with properties significantly different from those forming at semiconductor interfaces. Interestingly, 2DEG in oxides show a significant increase in electron density and strong electron correlation, with consequences in magnetic properties, superconductivity, ferroelectricity, and spin-orbit interaction [2,3]. Intrinsically, the electronic structure of 2DEG in oxide interfaces is different from the most standard semiconductor counterparts. In most of the oxide interfaces, the transport properties are dominated by narrow d -band electrons, whereas in semiconductors the electrons localized at states at the bottom of the conduction band dictate the properties of the 2DEGs. However, despite the great advance in the understanding of 2DEG in complex oxide interfaces, still many oxide interfaces are challenging to characterize, mainly because of their crystal quality. Analysis of the

electronic structure is commonly achieved by angle-resolved photoemission spectroscopy (ARPES). However, ARPES characterization requires high-quality, large and flat crystals. For instance, high-quality crystals of bismuthates were obtained, allowing detailed characterization by ARPES and revealing the mechanism of its high temperature superconductivity, an open discussion for more than 30 years [4].

Moreover, the formation of 2DEG with high mobility in amorphous oxides has motivated increasing interest [5,6]. The origin of the 2DEG formation at these interfaces has been assigned to electronic reconstruction via interfacial charge transfer [7]; however, detailed characterization of the properties of 2DEGs formed by amorphous oxides is still lacking. An alternative to ARPES characterization is to analyze the optical conductivity of the 2DEGs by polarized spectroscopy techniques such as spectroscopic ellipsometry. Although structural distortion and defects in amorphous materials may cause complex dielectric screening and significantly complicate the analysis of the properties of the 2DEG, a theoretical model can be assessed and improved by direct feedback from optical characterization [8].

Here, we report on midinfrared ellipsometry characterization of the properties of 2DEG formed at the interface between a nonmagnetic metal and amorphous semiconducting oxide, Cu/Bi₂O₃. Recent spin-charge interconversion experiments suggest the presence of a 2DEG with spin-orbit coupling (SOC) at this interface [9–11], making it a very attractive structure for spin-based complementary metal-oxide semiconductor technologies [12,13]. The characterization by angle-resolved ellipsometry confirms the formation of a 2DEG with

*jmflores@cactus.iico.uaslp.mx

†jorgeluis.pueblanunez@riken.jp

Thermal contrast of active dynamic thermography versus static thermography

Francisco Javier González^{a,b,*}, Raymundo González^a and Juan Carlos López^a

^a *Higia, Inc., Cerrada Buenavista 17, Fracc. Vista del Volcán, Puebla, 72154, Mexico*

^b *LANCYTT/UASLP, Sierra Leona 550, San Luis Potosi, SLP, 78210, Mexico*

Abstract. The use of steady state thermal patterns in breast cancer screening have shown low specificities, it is believed that by thermally exciting the body with a cold stimulus the temperature contrast will increase as well as the specificity of the technique. In this work computer thermal simulations of breasts subjected to a cold stress and at steady state were performed on a real scanned human female model in order to evaluate the advantages of using active dynamic thermography over steady state thermography. Results show that there is an increase in contrast when performing active dynamic thermography compared to steady state thermography but only in the case of tumors that are close to the surface of the skin. It was also found that the morphology of the torso and breasts appears to play a role in the sensitivity of thermal measurements needed for tumor detection.

Keywords: Breast thermography, finite element simulations, active dynamic infrared thermography

1. Introduction

Several studies have associated thermal patterns of the breast with diverse breast pathologies. In general malignant pathologies of the breast show an asymmetric thermal profile, increased vascularity and localized regions with increased temperature, usually higher than 2°C, compared to their contralateral region of the breast [5].

Thermal patterns are recorded by taking temperature measurements of the skin using non contact methods such as infrared thermography or contact methods such as liquid crystal thermography or through the use of electronic sensors [8]. Steady state thermal measurements are performed after the body has been acclimatized to a specific temperature, usually around 25 degrees C, for 10–15 minutes [6,7].

Clinical reports on the use of steady state thermal patterns in breast cancer diagnosis have shown low specificities resulting in a large amount of false positives [9]. Active dynamic thermography consists in thermally exciting the target for a given time period and recording the temperature behavior of the body as a function of time. It is believed that by thermally exciting the body with a cold stimulus the temperature contrast will increase, making it easier to identify breast malignancies thus reducing false positives and false negatives, increasing the specificity of the technique [6].

Cooling methods such as alcohol applied directly to the breast, cooling by convection using fans and introducing hands and feet in cold water have been used as thermal excitation for active dynamic

*Corresponding author. E-mail: javier.gonzalez@uaslp.mx.

Dispositivo láser semiconductor con puntos cuánticos para emisión en el cercano infrarrojo

J.V. González-Fernández^{a,*}, R. Díaz de León-Zapata^b, I. Lara-Velázquez^b and J. Ortega-Gallegos^c

^aUnidad Especializada en Energías Renovables del Tecnológico Nacional de México/IT La Laguna, Blvd. Revolución y Calzada Cuauhtémoc s/n, 27000, Torreón, Coahuila, México.

*e-mail: fanogf@gmail.com

^bTecnológico Nacional de México/IT San Luis Potosí,

Av. Tecnológico s/n, C.P. 78437, Soledad de Graciano Sánchez, SLP, México.

^cInstituto de Investigación en Comunicación Óptica, Universidad Autónoma de San Luis Potosí,

Av. Karakorum 1470, Lomas 4^a sección, 78210, San Luis Potosí, SLP, México.

Received 7 July 2018; accepted 3 September 2018

En este trabajo se reporta la fabricación de un dispositivo láser de semiconductores III-V de confinamiento separado. La heteroestructura se creó usando la técnica de epitaxia por haces moleculares y se caracterizó óptica, topográfica y eléctricamente por medio de fotoluminiscencia, microscopía de tunelamiento, electroluminiscencia, relaciones de corriente-voltaje y corriente-potencia, respectivamente. El confinamiento electrónico es llevado a cabo por un emparedamiento del área activa con pozos cuánticos de InGaAs con una composición que permite un acople estructural entre el pozo cuántico y los puntos cuánticos autoensamblados de InAs disminuyendo las dislocaciones que darían lugar a una mala calidad del dispositivo. El objetivo es obtener una emisión láser en las ventanas de menor absorción de las fibras ópticas situadas en el cercano infrarrojo en las que se basan los sistemas de telecomunicación.

Descriptores: Puntos cuánticos; dispositivos semiconductores; epitaxia por haces moleculares; láser.

In this work the fabrication of III-V semiconductor laser device with separate confinement is reported. The heterostructure was grown by molecular beam epitaxy technique and it was characterized by optical, morphological and electrical techniques such as photoluminescence, scanning tunneling effect, electroluminescence, current-voltage and current-power relations, respectively. The electronic confinement was carried out by sandwiching the active area with InGaAs quantum well with an appropriated Indium composition that allows a structural coupling between quantum wells and self-assembled InAs quantum dots decreasing dislocations that could commit the device quality. Our aim is to obtain the laser emission in the lower absorption windows for optical fiber telecommunications systems located in the near-infrared.

Keywords: Quantum dots; semiconductor devices; molecular beam epitaxy; laser.

PACS: 78.67.Hc; 42.55.Px; 81.15.Hi.

1. Introducción

Los materiales semiconductores del grupo III-V han sido ampliamente utilizados y estudiados para el desarrollo de dispositivos electroópticos como diodos emisores de luz (LED's) y láseres [1-4], que de manera convencional se fabrican mediante la deposición de películas semiconductoras delgadas por técnicas como epitaxia por haces moleculares (MBE) o por epitaxia metalorgánica en fase de vapor (MOCVD) [5-7]. Las investigaciones dirigidas al desarrollo e innovación de las tecnologías para las telecomunicaciones demandan una mejora continua y son de considerable importancia, en particular en lo que se refiere a los procesos de transmisión y recepción de datos. Varias líneas de investigación continúan en la dirección de los dispositivos pasivos de los sistemas de telecomunicaciones, como por ejemplo en la reducción de la absorción por medio de dopajes en las fibras ópticas, así como el aumento en la calidad de estas líneas de transmisión, pero la mayor parte de los esfuerzos se centran en el desarrollo de los dispositivos ópticos emisores de luz con las características propias de los láseres.

Para la fabricación de láseres de confinamiento separado es necesario depositar una sección cuya función es mantener

confinada la luz en una cavidad reflectora y otra sección en la que los electrones experimenten un confinamiento debido a la presencia de una barrera de potencial que se genera al depositar una capa de un semiconductor con una banda de energía prohibida lo suficientemente mayor para que el efecto de confinamiento de portadores sea efectivo [8]. Para lograr obtener un láser cuya emisión de la zona activa esté centrada en las ventanas de menor absorción para telecomunicaciones por fibra óptica (1.3 y 1.55 μm) [9,10], es necesario recurrir a defectos controlados que conforman sistemas de confinamiento electrónico como pozos o puntos, cuya geometría deriva en propiedades cuánticas que permiten obtener dispositivos con características ópticas apropiadas para este fin.

El espectro de emisión mejora ampliamente cuando los electrones son confinados en dos dimensiones por medio de pozos cuánticos, sin embargo, el semiancho de la forma de línea del espectro energético de la emisión disminuye si este se confina en tres dimensiones al insertar puntos cuánticos auto-ensamblados de manera que la eficiencia del dispositivo aumenta considerablemente al mismo tiempo que disminuye la temperatura de trabajo y la corriente de umbral [11,12]. La fabricación de estas heteroestructuras es complicada debido a la dinámica de difusión del Indio que provoca gradientes de



QUANTUM WELLS BASED STRUCTURES TESTED BY PHOTOREFLECTANCE ANISOTROPY SPECTROSCOPY AT ROOM TEMPERATURE

ESTRUCTURAS BASADAS EN POZOS CUÁNTICOS ANALIZADAS POR FOTORREFLECTANCIA ANISOTRÓPICA A TEMPERATURA AMBIENTE

J.V. González-Fernández^{1*}, R. Díaz de León-Zapata¹, E. Flores-García¹, J. Ortega-Gallegos²

¹Tecnológico Nacional de México/IT de San Luis Potosí, Av. Tecnológico s/n, CP 78437, Soledad de Graciano Sánchez, SLP, México.

²Instituto de Investigación en Comunicación Óptica, Universidad Autónoma de San Luis Potosí, Av. Karakorum 1470, Lomas 4ª sección, CP 78210, San Luis Potosí, SLP, México.

Received: July 3, 2018; Accepted: September 27, 2018

Abstract

We report the visualization of interface optical anisotropies in III-V semiconductor based coupled double quantum wells by using photoreflectance anisotropy spectroscopy. Interfacial optical anisotropies were detected from buried layers with quantum dimensions at room temperature through a piezoelectric shear strain. The discrete transitions associated to coupled double quantum wells were observed in near-infrared range, specifically in the second telecommunication band. We propose to use this extended photoreflectance spectroscopy through a polarization contrast as a simple and complementary optical method for analyzing anisotropic quantum structures with polarizable defects or anti-symmetries.

Keywords: semiconductors, photoreflectance, quantum wells, optical anisotropies.

Resumen

Se reporta la detección de anisotropías ópticas interfaciales de pozos cuánticos dobles acoplados basados en semiconductores III-V por medio de la espectroscopía de fotorreflectancia anisotrópica. Las anisotropías corresponden a películas no superficiales y de dimensiones cuánticas detectadas a través de un esfuerzo piezoeléctrico de cizalla en condiciones ambientales. Las transiciones discretas asociadas a los pozos acoplados se encuentran en el rango del cercano infrarrojo, específicamente en la segunda banda de menor absorción de telecomunicaciones. Se propone usar la técnica de fotorreflectancia extendida por contraste de polarización como un método óptico simple y complementario para analizar estructuras cuánticas con defectos polarizables o antisimetrías.

Palabras clave: semiconductores, fotorreflectancia, pozos cuánticos, anisotropías ópticas.

1 Introduction

Over the years, complex semiconductor devices such as lasers, solar cells, photodetectors or optical switches, for instance, have been improved using low dimensional structures as for instance quantum well, dots or wires due to their quantum properties (Huwer *et al.*, 2017; Li, 2017; Mukhtarova *et al.*, 2016; Wierer, Koleske, & Lee, 2012; Zheng, Gan, Zhang, Zhuge, & Zhai, 2017). For optical fiber communications devices, the semiconductor active zone must be optimized for low absorption window (1.3?1.55 ?m). Multiple alloys and quantum size structures are combined and used for achieving this

goal. Coupled double quantum wells (CDQWs) have attracted much attention due to interesting electronic properties and the formation of suitable energy levels, for example in near and mid infrared. In CDQWs, the electronic properties are then further modified by their coupling barrier width. When the barrier thickness changes a little bit, for example 1 monolayer, the lower energy level change too. The thickness of the coupling barrier could work as a tuning parameter for interband energy transitions. The research about CDQWs is going to reduce stress, strain or defects in semiconductor devices. CDQW structures based on III-V semiconductor alloys have been characterized by a number of techniques, for example electroreflectance, absorbance, transmittance,

* Corresponding author. E-mail: fanogf@gmail.com

<https://doi.org/10.24275/uam/izt/dcbi/revmexingquim/2019v18n3/Gonzalez>
issn-e: 2395-8472



Research articles

Magnetic properties of GaAs:Mn self-assembled nanostructures grown at relatively high-temperature by Molecular Beam Epitaxy

A. del Rio-de Santiago^{a,b,*}, C.F. Sánchez-Valdés^c, J.L. Sánchez Llamazares^d, M.A. Vidal^b, V.H. Méndez-García^b, M. López-López^e, E. Cruz-Hernández^{b,*}

^a Unidad Académica de Ingeniería, Universidad Autónoma de Zacatecas, Ramón López Velarde 801, C.P. 98000 Zacatecas, Zac., Mexico

^b Coordinación para la Innovación y Aplicación de la Ciencia y Tecnología (CIACyT), Universidad Autónoma de San Luis Potosí (UASLP), Av. Sierra Leona #550, Lomas 2a Sección, San Luis Potosí, S. L. P. 78210, Mexico

^c División Multidisciplinaria, Ciudad Universitaria, Universidad Autónoma de Ciudad Juárez (UACJ), Calle José de Jesús Macías Delgado # 18100, Ciudad Juárez 32579, Chihuahua, Mexico

^d Instituto Potosino de Investigación Científica y Tecnológica A.C., Camino a la Presa San José 2055, Col. Lomas 4^a sección, San Luis Potosí, S.L.P. 78216, Mexico

^e Physics Department, Centro de Investigación y de Estudios Avanzados del IPN, Apartado Postal 14-740, México D.F. 07000, Mexico



ARTICLE INFO

Keywords:

Magnetic cluster
Self-assembly
Diluted magnetic semiconductor
Nanostructures

ABSTRACT

We report the influence of the Mn atomic concentration (at.%) on the nanostructures formation and magnetic properties of GaAs:Mn layers grown by Molecular Beam Epitaxy at a relatively high substrate temperature of 530 °C varying the nominal Mn at.% content from 0.01 to 0.2. It is shown that by modifying the Mn at.% different kind of nanostructures, ranging from 2D (such as islands and surface corrugation) to 3D microleaved and nanowire-like arrays, form on the surface layer. Samples produced with Mn contents ranging from 0.02 to 0.20 at.% show a significant room temperature ferromagnetic response that is attributed to the formation of MnAs nanocrystals as confirmed from X-ray diffraction analysis and magnetization measurements. The influence of MnAs clusters on the formation of the nanostructures observed is discussed.

1. Introduction

The synthesis of semiconducting alloys presenting ferromagnetic behavior is of considerable current interest because it could be the basis for joining two large branches of Materials Science, semiconductors and ferromagnetic materials [1]. Potentially, this could give rise to the development of devices using both degrees of freedom, such as magnetic random-access memories, field-effect transistors, diodes or even solar cells [2–4]. For such applications, (Ga,Mn)As is one of the so-called diluted magnetic semiconductors (DMS) that has been subject of extensive attention in the last few years [5]. In spite of the low solubility of Mn into the GaAs matrix at the growth temperatures usually employed to grow GaAs epitaxial layers by Molecular Beam Epitaxy (MBE) (i.e., around 600 °C), by growing at low temperatures (below 300 °C) have been possible to fabricate (Ga,Mn)As with Mn concentration many times higher than its solubility limit [6]. Following this low temperature MBE method, (Ga,Mn)As samples presenting a Curie temperature (T_C) around 200 K has been achieved [7]. However, in spite of the considerable efforts carried out to optimize growth

parameters and post-growth thermal treatments it seems that a further increase in the T_C of (Ga,Mn)As is unlikely [7].

The formation of Mn-rich (Ga,Mn)As or MnAs nanoclusters integrated into the GaAs matrix have been also receiving increasing attention due to the observation of interesting room-temperature magneto-optical and magnetoresistance effects [8,9]. In fact, it has been reported that even at a low Mn content, Mn-rich (Ga,Mn)As nanoclusters embedded into the GaAs matrix synthesized by growing at low (250 °C) or moderate (350 °C) temperatures followed by a thermal annealing treatment at 500–650 °C, can exhibit a ferromagnetic response with a T_C as high as 360 K [9,10]. On the other hand, as semiconductor nanostructures possess important quantum effects and applications [11], the surfactant properties of Mn could be advantageous to self-assemble (Ga,Mn)As-based nanostructures presenting both, magnetic response and quantum confinement.

Early studies have been focused mainly on (Ga,Mn)As-based wire-shaped nanostructures. Nanowires were first obtained in layered (Ga,Mn)As structures produced by e-beam lithography [12]. First reports on the effect of catalytic properties of Mn in the growing of

* Corresponding authors at: Coordinación para la Innovación y Aplicación de la Ciencia y Tecnología (CIACyT), Universidad Autónoma de San Luis Potosí (UASLP), Av. Sierra Leona #550, Lomas 2a Sección, San Luis Potosí, S. L. P. 78210, Mexico (E. Cruz-Hernández).

E-mail addresses: risa008537@uaslp.mx (A. del Rio-de Santiago), esteban.cruz@uaslp.mx (E. Cruz-Hernández).

<https://doi.org/10.1016/j.jmmm.2018.12.030>

Received 2 August 2018; Received in revised form 30 November 2018; Accepted 9 December 2018

Available online 10 December 2018

0304-8853/ © 2018 Elsevier B.V. All rights reserved.

Characterization of n-GaN / p-GaAs NP heterojunctions

C. A. Hernández-Gutiérrez¹, Y. L. Casallas-Moreno², Dagoberto Cardona³, Yu. Kudriavtsev⁴, G. Santana-Rodríguez⁵, R. Mendoza-Pérez⁶, G. Contreras-Puente⁷, V. H. Mendez-García⁸, S. Gallardo-Hernández⁹, M.A. Quevedo-Lopez¹, M. López-López⁹.

¹ Department of Materials Science and Engineering, University of Texas at Dallas, Richardson, TX 75080, USA.

² Unidad Profesional Interdisciplinaria en Ingeniería y Tecnologías Avanzadas, Instituto Politécnico Nacional, Av. IPN 2580, Gustavo A. Madero, 07340 Ciudad de México, México.

³ Mathematics and Physics Department, ITESO, Periférico Sur Manuel Gómez Morín # 8585, C.P. 45604 Tlaquepaque, Jalisco, Mexico.

⁴ Department of Electrical Engineering–SEES, Cinvestav-IPN, México, DF, 07360, Ciudad de México, México.

⁵ National Autonomous University of Mexico UNAM, Coyoacán, DF, C.P. 04510, Ciudad de México, México.

⁶ Autonomous University of Mexico City, Iztapalapa, C.P. 09790, Ciudad de México, México.

⁷ National Polytechnic Institute, ESFM, 07738, Ciudad de México, México.

⁸ National Laboratory, CIACyT-UASLP, Av. Sierra Leona #550, Col. Lomas 2a. Sección C.P. 78210, San Luis Potosí, S.L.P., México.

⁹ Physics Department, Cinvestav-IPN, México, DF, 07360, Ciudad de México, México.

n-GaN/p-GaAs heterojunctions were fabricated by plasma-assisted molecular beam epitaxy (PA-MBE). The fabrication was carried out by the growth of n-type cubic GaN on p-type GaAs(100) substrates, followed by Ohmic contact deposition using conventional e-beam and rapid thermal annealing. With the n-GaN/p-GaAs heterojunction we have obtained photovoltaic effect and demonstrated that this effect strongly depends of the GaN nucleating layer on the GaAs surface. Likewise, we found that the decrease of hexagonal-stable phase and planar defects inclusions in the cubic-metastable GaN decreases the leakage current, and therefore, increases the open circuit voltage (Voc). Furthermore, the increase in crystal quality also increases the External quantum efficiency (EQE) at longer wavelengths due to the reduction of surface recombination velocity at the GaN/GaAs interface. In addition, the heterojunctions were tested as radiation detectors, demonstrating that they could be a candidate for alpha particle detectors if the thickness of the absorber layer is increased.

Keywords: Cubic phase, GaN, GaAs, heterojunction, photovoltaic applications, Photodetector.



The Decoration of Gold Core in Au@ZrO₂ Nanoreactors with Trace Amounts of Pd for the Effective Reduction of 4-Nitrophenol to 4-Aminophenol

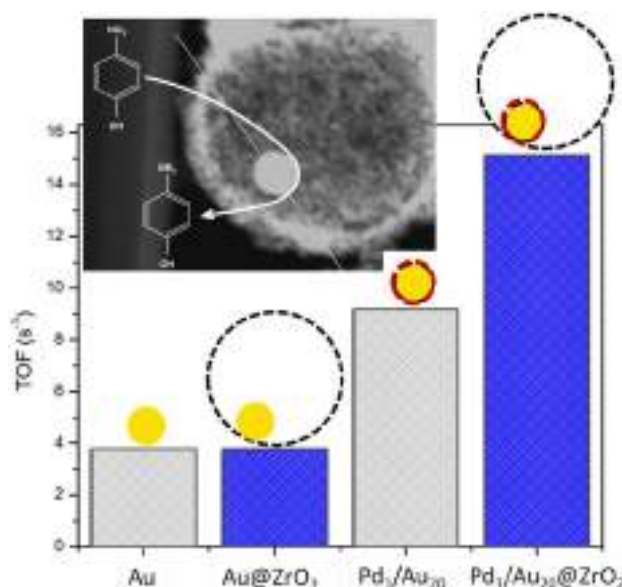
Brenda Acosta^{1,2,3} · Viridiana Evangelista² · Serguei Miridonov⁴ · Sergio Fuentes³ · Andrey Simakov³

Received: 6 December 2018 / Accepted: 24 March 2019
© Springer Science+Business Media, LLC, part of Springer Nature 2019

Abstract

Pd₁/Au₂₀@ZrO₂ nanoreactors with the gold nuclei confined within zirconia shell and decorated with Pd were synthesized using an Au:Pd molar ratio of 20:1. The presence of even trace amounts of Pd on the gold nuclei surface, significantly enhanced catalytic activity of Pd₁/Au₂₀@ZrO₂ nanoreactors in the 4-nitrophenol to 4-aminophenol transformation by four times compared to Au@ZrO₂. In addition, the Pd₁/Au₂₀@ZrO₂ nanoreactors remained highly stable during the reaction even under harsh conditions, i.e. without nanoreactors cleaning before the subsequent catalytic run, comparable with the stability of Au@ZrO₂ nanoreactors. The presently proposed synthesis technique allowed to prepare nanoreactors of uniform structure even with relatively unstable bimetallic NPs (Pd/Au) as nuclei.

Graphical Abstract



Keywords Nanoreactors · Bimetallic Pd/Au · Decoration · 4-Nitrophenol reduction · High stability

Electronic supplementary material The online version of this article (<https://doi.org/10.1007/s10562-019-02758-y>) contains supplementary material, which is available to authorized users.

Extended author information available on the last page of the article

1 Introduction

Metal nanoparticles (NPs) confined within mesoporous shells have become attractive for numerous applications due to the advantages provided by the shell (stability of the metal

Topical Review

The 2019 surface acoustic waves roadmap

Per Delsing¹, Andrew N Cleland², Martin J A Schuetz³, Johannes Knörzer⁴, Géza Giedke^{5,6}, J Ignacio Cirac⁴, Kartik Srinivasan⁷, Marcelo Wu^{7,8}, Krishna Coimbatore Balram^{7,9}, Christopher Bäuerle¹⁰, Tristan Meunier¹⁰, Christopher J B Ford¹¹, Paulo V Santos¹², Edgar Cerda-Méndez¹³, Hailin Wang¹⁴, Hubert J Krenner^{15,16,30}, Emeline D S Nysten¹⁵, Matthias Weiß¹⁵, Geoff R Nash¹⁷, Laura Thevenard¹⁸, Catherine Gourdon¹⁸, Pauline Rovillain¹⁸, Max Marangolo¹⁸, Jean-Yves Duquesne¹⁸, Gerhard Fischerauer¹⁹, Werner Ruile²⁰, Alexander Reiner¹⁵, Ben Paschke¹⁵, Dmytro Denysenko^{15,28}, Dirk Volkmer¹⁵, Achim Wixforth^{15,16}, Henrik Bruus²¹, Martin Wiklund²², Julien Reboud²³, Jonathan M Cooper²³, YongQing Fu²⁴, Manuel S Brugger¹⁵, Florian Rehfeldt²⁵ and Christoph Westerhausen^{15,16,26,27,28}

¹ Microtechnology and Nanoscience, Chalmers University of Technology, 412 96 Göteborg, Sweden

² Institute for Molecular Engineering, University of Chicago, Chicago, IL 60637, United States of America

³ Physics Department, Harvard University, Cambridge, MA 02318, United States of America

⁴ Max-Planck-Institut für Quantenoptik, Hans-Kopfermann-Strasse 1, 85748 Garching, Germany

⁵ Donostia International Physics Center, Paseo Manuel de Lardizabal 4, E-20018 San Sebastián, Spain

⁶ Ikerbasque Foundation for Science, Maria Diaz de Haro 3, E-48013 Bilbao, Spain

⁷ National Institute of Standards and Technology, Gaithersburg, MD 20899-6203, United States of America

⁸ University of Maryland, College Park, MD 20742, United States of America

⁹ Department of Electrical and Electronic Engineering, University of Bristol, Bristol BS8 1UB, United Kingdom

¹⁰ Univ. Grenoble Alpes, CNRS, Institut Néel, Grenoble, France

¹¹ Cavendish Laboratory, University of Cambridge, Cambridge, United Kingdom

¹² Paul-Drude-Institut für Festkörperelektronik, Berlin, Germany

¹³ Universidad Autónoma de San Luis Potosí, San Luis Potosí, Mexico

¹⁴ University of Oregon, OR, United States of America

¹⁵ Institute of Physics, University of Augsburg, 86159 Augsburg, Germany

¹⁶ Nanosystems Initiative Munich (NIM), Munich, Germany

¹⁷ The University of Exeter, Exeter, United Kingdom

¹⁸ Sorbonne Université, CNRS, Institut des Nanosciences de Paris, 4 place Jussieu 75252 Paris, France

¹⁹ Universität Bayreuth, Bayreuth, Germany

²⁰ RF360 Europe GmbH, Munich, Germany

²¹ Department of Physics, Technical University of Denmark, Kongens Lyngby, Denmark

²² Department of Applied Physics, Royal Institute of Technology, Stockholm, Sweden

²³ School of Engineering, University of Glasgow, G12 8LT, Glasgow, United Kingdom

²⁴ Faculty of Engineering and Environment, Northumbria University, NE1 8ST, Newcastle upon Tyne, United Kingdom

²⁵ University of Göttingen, 3rd Institute of Physics—Biophysics, Germany

²⁶ Center for NanoScience (CeNS), Ludwig-Maximilians-Universität Munich, 80799 Munich, Germany

²⁷ The Center for Interdisciplinary Health Research (ZIG), University of Augsburg, 86135 Augsburg, Germany

²⁸ Augsburg Center for Innovative Technologies (ACIT), Augsburg 86159, Germany

²⁹ This author is sadly now deceased. This Roadmap is dedicated to him.

³⁰ Author to whom any correspondence should be addressed.



Original content from this work may be used under the terms of the [Creative Commons Attribution 3.0 licence](https://creativecommons.org/licenses/by/3.0/). Any further distribution of this work must maintain attribution to the author(s) and the title of the work, journal citation and DOI.

Wavelet singularity analysis for CAP sleep delineation

David Israel Medina
Facultad de Ciencias
Universidad Autónoma de San Luis
Potosí
San Luis Potosí (SLP), México
davidmedinai@hotmail.com

Martin O. Mendez
Laboratorio Nacional CI3M
Facultad de Ciencias
Universidad Autónoma de San Luis
Potosí
San Luis Potosí (SLP), México
mmendez@fc.uaslp.mx

Ioanna Chouvarda
School of Medicine
Aristotle University of Thessaloniki
Thessaloniki, Greece
ioannach@auth.gr

J. S. Murguía
Laboratorio Nacional CI3M
Facultad de Ciencias
Universidad Autónoma de San Luis
Potosí
San Luis Potosí (SLP), México
ondeleto@uaslp.mx

Abstract— Sleep is an essential process in our life, which covers 1/3 of our lifetime. But this process can be affected by disorders producing serious consequences at physiological and behavioral level. One of the major indexes connected to the sleep disorders is the dynamic of the sleep macrostructure that is used for the assessment of sleep quality. Beyond sleep macrostructure, recently attention is also given to a finer structure of sleep called Cyclic Alternating Pattern (CAP). CAP is composed by short cortical events (A-phases), where some transition processes can be observed. With the aim to unveil properties of this transition phenomenon, in this work, we present a wavelet singularity analysis of the EEG signal during the onset and offset of A-phases. The results showed that EEG signal presents significant differences between A-phases and activity of background when the average singularity is considered. This finding can help both in better delineating the A-phases of CAP sleep and in understanding the mechanisms behind the CAP dynamics.

Keywords—A-phase, Hölder exponent, CAP sleep, singularity.

I. INTRODUCTION

Sleep is a fundamental process for the human being. Basic processes as memorization, resting, growing, etc. take place during the sleep process. However, there exist many questions related to sleep, and with the intention of understanding it better, many studies have dedicated efforts to analyze the electrical information of the brain during sleep. This has allowed new knowledge in the interpretation of sleep in normal and pathologic conditions, and nowadays, it is well known that a fragmented sleep could have side effects and generates metabolic syndrome [1], irritability, lack of concentration and traffic accidents [2, 3].

The Polysomnography (PSG) is the clinical gold standard to evaluate the sleep. During the PSG, some electrophysiological signals are recorded: electroencephalogram (EEG), electrooculogram, and electromyogram. These signals are used to annotate the sleep stages (wake, 1-4 and REM) on nonoverlapping segments of 30s. The definition of each sleep stage takes mainly on consideration the frequency content of the signals and the sleep is principally characterized by the sleep stages [4]. However, an oscillatory brain pattern composed by short

events has been recently studied, there is evidence of a large correlation with the dynamic of the sleep stages, and in maintaining a sleep stage (i.e., sleep stage 4) and in the generation of the sleep stage transitions [5]. These short events present duration between 2s and 60s and these can be identified as oscillations, called A-phases, which disrupt the sleep stages EEG rhythms. A-phases can be grouped in three types based on spectral characteristics and durations, as described below:

- A1 phase. Characterized by bursts and K-complexes of Delta waves (0.5 Hz - 4 Hz). An example is depicted in Figure 1.
- A2-phase. Presents rapid EEG waves (Alpha (8 Hz - 12 Hz) and Beta (12 Hz - 30 Hz)) that cover between 20% and 50% of the A-phase duration and the Delta waves in the rest of the event duration.
- A3-phase. Characterized by Alpha and Beta waves, which occupy more than 50% of the A-phase duration.

A-phases present a dynamic and following some rules, the oscillatory sleep pattern named the Cyclic Alternating Pattern (CAP), is obtained [5]. The CAP rate is computed based on the ratio of time in CAP with respect to the sleep time. CAP rate is a quantitative clinical index used to measure the sleep quality [6]. However, even if CAP rate is an important clinical index for sleep evaluation, A-phases annotation is a handmade and tedious procedure. These produce large subjectivity and high inter-scoring variability [7]. To mitigate the problems generated with the annotations and trying to give a mathematical definition of the A-phase, some researches have studied the properties of the A-phases and their surroundings by using spectral decomposition and complexity measures [8, 9], and interesting results were obtained. However, the A-phase definition mentions a disruption of the basal EEG oscillations that characterize the sleep stage. This means that the clinician observes an abrupt signal change in frequency or amplitude when an A-phase occurs. Thus, it could be interesting to know if there locally exists a smooth transition or a sudden transition, and this will give new insight about the

Partial Image Encryption Using Cellular Automata

Marco Tulio Ramírez Torres¹, Marcela Mejía Carlos², José S. Murguía Ibarra³, Luis Javier Ontañón García¹

¹ Universidad Autónoma de San Luis Potosí, CARAO,
México

² Universidad Autónoma de San Luis Potosí, IICO,
México

³ Universidad Autónoma de San Luis Potosí,
Facultad de Ciencias,
México

{tulio.torres, marcela.mejia, ondeleto, luis.ontanon}@uaslp.mx

Abstract. In this work is proposed a partial image encryption method based on the synchronization of the cellular automaton rule 90. The security analysis proves that this cryptosystem is resistant to different tests and attacks such as the Chosen/Knownplain image attack and bit-replacement. This algorithm is a variant from another encryption algorithm named ESCA, in this case we modified the ESCA system to a partial encryption version reducing the latency time up to a 50%. This version has two changes a) it only encrypts the three most significant bits, and b) the bits of the secret key are rotated instead of calculating a key for each block of plaintext. These changes allow to reduce the latency time and according to the tests do not compromise the security. This proposal could be a feasible and secure option for real-time applications.

Keywords. Partial encryption, digital images, cellular automata.

1 Introduction

Nowadays, many of our information is in digital formats and it is sent through networks or is stored in different devices. And, with technologies as Internet of things our personal data could be more and more exposed, therefore we need to learn about internet and its risks [14] and develop new security techniques. For this reason, it exists a great interest in the protection and manipulation of the data.

Due to the great advances in technology, each time is required to have better and more efficient algorithms for confidential and secure data handling. This information may vary depending on the application area and in many cases is necessary processing it in real time.

For example, pictures, medical images, diagrams, surveillance video, video conference, etc. could contain confidential information, and if these data are transmitted and are not encrypted the confidentiality of information is exposed in the links allowing access to third parties without being detected. To overcome the eavesdropping problem several encryption systems have been proposed, such as AES (Advanced Encryption Standard), IDEA (International Data Encryption Algorithm), RSA (Rivest, Shamir y Adleman) among others.

These systems are generally used in text and binary data, but they are not suitable for the encryption of multimedia content as digital images and audio files, due to their massive volumes, high adjacent correlation and sometimes the multimedia data require real-time interactions (displaying, bit rate conversion, etc.) [3]. That is why the image encryption is a particular studying area. The image encryption algorithms should provide two kinds of security: cryptographic security and perceptual security.

Soliton Molecules in Self-Mode-Locked Ring-Cavity Er/Yb Double-Clad Fiber Laser

(Invited Paper)

Manuel Durán-Sánchez ^{1,2}, Berenice Posada-Ramírez ¹,
Ricardo Iván Álvarez-Tamayo ³, Héctor Santiago-Hernández,⁴
Miguel Bello-Jiménez ⁵, Baldemar Ibarra-Escamilla ¹,
Shyamal Das,⁶ Anirban Dhar,⁶ Mrinmay Pal,⁶ Mukul Chandra Paul,⁶
Alexander V. Kir'yanov ^{7,8} and Evgeny A. Kuzin¹

¹Instituto Nacional de Astrofísica, Óptica y Electrónica, Puebla 72824, Mexico

²CONACyT—Instituto Nacional de Astrofísica, Óptica y Electrónica, Puebla 72824, Mexico

³CONACyT—Universidad Autónoma de Nuevo León, San Nicolás de los Garza 66451, Mexico

⁴Departamento de Electrónica, Universidad de Guadalajara, Guadalajara 44840, México

⁵Instituto de Investigación en Comunicación Óptica, Universidad Autónoma de San Luis Potosí, San Luis 78210, México

⁶Fiber Optics and Photonics Division, CSIR-Central Glass and Ceramic Research Institute, Kolkata 700032, India

⁷Centro de Investigaciones en Óptica, León 37150, México

⁸National University of Science and Technology "MISIS", Moscow 119049, Russia

DOI:10.1109/JPHOT.2019.2943075

This work is licensed under a Creative Commons Attribution 4.0 License. For more information, see <https://creativecommons.org/licenses/by/4.0/>

Manuscript received June 4, 2019; revised September 12, 2019; accepted September 17, 2019. Date of publication September 23, 2019; date of current version October 11, 2019. This work was supported by Consejo Nacional de Ciencia y Tecnología (CONACyT) under Grant CB-256401. Corresponding author: Manuel Durán-Sánchez (e-mail: manuedl@inaoep.mx).

Abstract: In this paper, generation of soliton molecules by a self-mode-locked Er/Yb double clad fiber laser is experimentally demonstrated. The optical spectrum of the bound solitons exhibits eight well defined peaks at ~ 1563 nm with high modulation depth. The corresponding autocorrelation measurement shows a fundamental trace with several narrow peaks, suggesting the presence of bound solitons. The obtained results demonstrate the reliability of our simple laser configuration for the formation of more robust soliton molecules as the pump power is increased. The soliton molecules exhibit repetition rate of 19.54 MHz and average power of 1.2 W, achieved with a pump power of ~ 4.8 W.

Index Terms: Fiber laser, mode-locked lasers, pulse propagation and temporal solitons.

1. Introduction

Passively mode-locked fiber lasers as simple and low-cost coherent sources with ultrashort pulsed emission are attractive for a wide range of applications including: fiber sensing, laser measurement, nonlinear optical properties of materials, spectroscopy, and optical communications, among others [1]–[4]. In order to obtain mode-locked laser operation in fiber lasers, different material-based fast saturable absorbers (SA) such as carbon nanotubes, semiconductor saturable absorber mirror, graphene, and topological insulators, have been extensively investigated. In this regard, another reliable technique to obtain mode-locked laser pulses, usually named

Stable Multi-Wavelength Thulium-Doped All-Fiber Laser Incorporating a Multi-Cavity Fabry–Perot Filter

A. Camarillo-Avilés,¹ D. Jauregui-Vazquez^{1,2},
J. M. Estudillo-Ayala^{1,2}, E. Hernández-Escobar,¹
J. M. Sierra-Hernández^{1,2}, O. Pottiez^{1,3}, M. Durán-Sánchez^{1,4,5},
B. Ibarra-Escamilla^{1,5} and M. Bello-Jiménez¹

¹Instituto de Investigación en Comunicación Óptica, Universidad Autónoma de San Luis Potosí, San Luis Potosí 78210, México

²Departamento de Electrónica, División de Ingenierías Campus Irapuato-Salamanca, Universidad de Guanajuato, Salamanca 36885, Mexico

³Centro de Investigaciones en Óptica, León 37150, México

⁴Consejo Nacional de Ciencia y Tecnología, Benito Juárez, 039040, México

⁵Departamento de Óptica, Instituto Nacional de Astrofísica, Óptica y Electrónica, Puebla 72000, México

DOI:10.1109/JPHOT.2019.2949500

This work is licensed under a Creative Commons Attribution 4.0 License. For more information, see <https://creativecommons.org/licenses/by/4.0/>

Manuscript received July 4, 2019; revised October 4, 2019; accepted October 21, 2019. Date of publication October 24, 2019; date of current version November 26, 2019. This work was supported by CONACyT “Fronteras de la Ciencia” under Grant 2438. Corresponding author: M. Bello-Jiménez (e-mail: miguel.bello@uaslp.mx).

Abstract: The present manuscript experimentally demonstrates multi-wavelength generation from a thulium-doped all-fiber laser by implementing a multi-cavity Fabry-Perot filter. The filter, with a composition that relies of several silica-air and air-silica interfaces, provide a spectral reflection response that allows the laser to be operated in single-, dual- or triple-wavelength emissions by simple and clear adjustment of the polarization state. In this way, the fiber laser is capable to operate over a broad range of wavelengths extending from 1844 to 1928 nm. In addition, dual-wavelength operations are also feasible in the 1844 and 1928 nm regions, exhibiting a mode spacing of 4.41 nm and 1.62 nm, respectively. Beside this, the laser is able to switch to a sextuple-wavelength operation regime in the 1885 nm region, maintaining a minimum wavelength spacing of 1.53 nm. The laser demonstrates high wavelength stability, with variations below 60 pm at all analyzed wavelengths, and a minimum peak power fluctuation of ± 2.77 dB.

Index Terms: Multi-wavelength, fiber laser, Fabry-Perot filter and thulium-doped fiber.

1. Introduction

All-fiber multi-wavelength thulium-doped fiber lasers (TDFLs) capable to operate near the 2- μ m region have received a great deal of attention in recent years; this has to do mainly with their potential of practical applications in science and industry [1]–[6]. At present, several approaches have been reported to perform stable multi-wavelength generation in TDFLs [7]–[20]. These methods include, for example, the use of Sagnac loop mirrors [7], [9], [15], [16], Fabry-Perot [18] or Mach-Zehnder [8], [11], [16] interferometers, specialty optical fibers [11], [19], mode-beating filters [7], [12], and four-wave mixing techniques [10], among others [13], [17], [20]. Recently, the fiber laser community have spent its efforts to develop fiber-optic devices operating in the 2- μ m region, as a consequence, new

Fiber laser with simultaneous multi-wavelength Er/Yb passively Q-switched and single-wavelength Tm gain-switched operations

J. ALANIZ-BAYLON,¹ M. DURÁN-SÁNCHEZ,^{1,2,*} R. I. ÁLVAREZ-TAMAYO,³ B. POSADA-RAMÍREZ,¹ M. BELLO-JIMÉNEZ,⁴ B. IBARRA-ESCAMILLA,¹ A. A. CASTILLO-GUZMAN,⁵ AND E. A. KUZIN¹

¹Instituto Nacional de Astrofísica, Óptica y Electrónica (INAOE), L. E. Erro 1, Sta. Ma. Tonantzintla, Pue. 72824, Mexico

²CONACyT-Instituto Nacional de Astrofísica, Óptica y Electrónica, A. P. 51 y 216, Pue. 72000, Mexico

³CONACyT—Universidad Autónoma de Nuevo León, Av. Universidad S/N, San Nicolás de los Garza, N. L. 66451, Mexico

⁴Instituto de Investigación en Comunicación Óptica, Universidad Autónoma de San Luis Potosí, Av. Karakorum 1470, S. L. P. 78210, Mexico

⁵Universidad Autónoma de Nuevo León, Av. Universidad S/N, San Nicolás de los Garza, N. L. 66451, Mexico

*Corresponding author: manued@inaoep.mx

Received 25 January 2019; revised 3 March 2019; accepted 12 March 2019; posted 14 March 2019 (Doc. ID 358697); published 3 May 2019

We report the experimental investigation of an all-fiber multi-wavelength passively Q-switched Er/Yb laser with simultaneous gain-switched pulsed operation by using a thulium-doped fiber as a saturable absorber. Laser emission is obtained in three wavelength regions with central peaks at around 1546 nm, 1561 nm, and 1862 nm. Multi-wavelength emission with separation of approximately 1 nm is obtained around the wavelength regions of 1546 nm and 1561 nm. Stable laser pulses are generated in the pump power range from 3.6 W to 7.3 W. © 2019 Chinese Laser Press

<https://doi.org/10.1364/PRJ.7.000608>

1. INTRODUCTION

Fiber lasers operating in wavelength regions of 1.5- μm and 2- μm have attracted great attention because of their potential applications in many research areas and industries such as medical surgery [1–3], optical communications [4], material processing [5], sensing and lidar [6,7], and spectroscopy [8], among others [9,10]. Among the techniques used to produce a pulsed light emission, Q-switching is one of the most preferred [11–19]. Q-switched fiber lasers can be designed to generate high-energy optical pulses with durations in the nanosecond range, which can be obtained by implementing both passive and active methods. In the last decade, passively Q-switched (PQS) operation of fiber lasers has been achieved by using un-pumped rare-earth-doped and co-doped fibers as fiber saturable absorbers (FSAs). This passive technique allows designing simple all-fiber laser systems [20]. In this technique, the laser configurations maintain advantages of cost-effectiveness, high efficiency, and free maintenance; in addition, no intra-cavity components are needed, which makes them compact and simple. Moreover, in recent years, gain switching (GS) has become a promising effective technique to obtain short high-energy laser pulses. GS laser operation is achieved by laser gain on–off commutation when a modulated pump source is used [21]. Then, the characteristics of the pulsed laser emission can be controlled, since the pulsed pump source directly modulates population inversion in the energy levels

of the gain medium [20]. In this regard, Q-switching lasers, used as pump sources, allow the generation of GS laser pulses to achieve pulsed high-energy light emission in the 2- μm region. Because of the different absorption bands of a Tm-doped fiber (TDF), GS laser emission near the 2- μm waveband can be achieved with a TDF laser (TDFL) with a modulated pump source at different operation wavelengths. Taking advantage of the in-band pump and absorption characteristics of the TDF, fast transition from $^3\text{H}_6$ energy level to the $^3\text{F}_4$ upper laser level can be reached. As a result, the cavity gain is switched on and off almost at the same time as the pump pulse [22], where stable GS laser pulse trains can be obtained, as reported in Refs. [23–26]. GS laser operation has been demonstrated by using a 1.55- μm modulated pump source, from which the shortest GS pulse of 10 ns was obtained in a scheme including a 20-cm-long TDF as the gain medium [23]. Approaches with simultaneous GS and mode-locking (ML) operation in Tm/Ho co-doped fiber laser configurations also have been reported [10,20]. Recently, our research group demonstrated a fiber laser setup with simultaneous Tm³⁺ PQS and Ho³⁺ GS operation [27].

In this paper, we experimentally demonstrate simultaneous PQS and GS operations of a fiber laser by using an Er/Yb double-clad fiber (EYDCF) and a TDF within the same linear cavity. Stable PQS pulses in the 1.55- μm wavelength region and GS pulses in the 1.8- μm region are obtained. The TDF



Gain-driven spectral-temporal noise-like pulse dynamics in a passively mode-locked fiber laser

O. POTTIEZ,^{1,*}  J. P. LAUTERIO-CRUZ,²  Y. E. BRACAMONTES-RODRÍGUEZ,¹ H. E. IBARRA-VILLALON,^{1,3}  J. C. HERNANDEZ-GARCIA,^{2,4} M. BELLO-JIMÉNEZ,⁵  AND E. A. KUZIN⁶ 

¹Centro de Investigaciones en Óptica, Lomas del Bosque 115, Col. Lomas del Campestre, León, Gto. 37150, Mexico

²Departamento de Electrónica, DICIS, Universidad de Guanajuato, Carr. Salamanca-Valle de Santiago km 3.5 + 1.8 km, Salamanca, Gto. 36885, Mexico

³Departamento de Ciencias Básicas, Universidad Autónoma Metropolitana-Unidad Azcapotzalco, Av. San Pablo No. 180. Col. Reynosa Tamaulipas, Azcapotzalco, CDMX, 02200, Mexico

⁴Consejo Nacional de Ciencia y Tecnología, Av. Insurgentes Sur No. 1582, Col. Crédito Constructor, Del. Benito Juárez, C.P. 039040, Mexico

⁵Instituto de Investigación en Comunicación Óptica (IICO), Universidad Autónoma de San Luis Potosí, Av. Karakorum No. 1470 Lomas 4aSecc., 78210 San Luis Potosí, Mexico

⁶Instituto Nacional de Astrofísica, Óptica y Electrónica, L.E. Erro 1, Sta. Ma. Tonantzintla, Pue. 72824, Mexico

*pottiez@cio.mx

Abstract: We study numerically complex noise-like pulse dynamics in a passively mode-locked erbium-doped fiber laser. Wavelength-dependent gain dynamics is modeled as a combination of a three-level and a four-level system, which approximate the gain behavior in the 1530-nm and 1560-nm regions, respectively. The typical deformation of the erbium gain spectrum as it saturates is properly reproduced by this approach. Several puzzling noise-like pulse dynamics that were recently observed experimentally are qualitatively reproduced numerically, in particular slow quasi-periodic energy variations and the emergence and walkoff of wavelength-shifted radiation components. These results clearly reveal that gain dynamics is deeply involved in the onset of such complex temporal and spectral instabilities in these sources.

© 2019 Optical Society of America under the terms of the [OSA Open Access Publishing Agreement](#)

1. Introduction

Although originally developed for the generation of stable trains of solitons, passively mode-locked fiber lasers are now increasingly regarded as an ideal platform to evidence and study a broad range of complex dynamics. These systems, in which dispersive, nonlinear and dissipative effects mingle and interact in intricate ways, constitute indeed the perfect stage where a broad spectrum of exotic scenarios are played out. These include, among others, soliton explosions [1], the emergence of extreme-intensity events known as optical rogue waves (ORWs) [2], as well as the formation and evolution of complex non-stationary waveforms: noise-like pulses (NLPs) [3–20]. NLPs are long (~ns) bunches of radiation characterized by a chaotic internal dynamics at sub-ps scale. Whereas some of their properties make them attractive for applications (including materials processing [21], medical imaging [22] or supercontinuum generation [23–25]), a precise understanding of their puzzling dynamics still challenges researchers. Recently, it was observed that the complex internal dynamics of NLPs was able to trigger the formation of ORWs [26–29]. In spite of its chaotic evolution at fine inner scale, a NLP can display a rather stable envelope through the bandwidth-limited optoelectronic measurement setup, and yield a steady train of pulses at the laser output, which is compatible with applications. In other instances, however, far



Experimental study of an in-fiber acousto-optic tunable bandpass filter for single- and dual-wavelength operation in a thulium-doped fiber laser

E. HERNÁNDEZ ESCOBAR,¹ M. BELLO JIMÉNEZ,^{1,*}  A. CAMARILLO AVILÉS,¹ R. LÓPEZ ESTOPIER,^{1,2} O. POTTIEZ,³  M. DURÁN SÁNCHEZ,^{2,4}  B. IBARRA ESCAMILLA,⁴  AND M. V. ANDRÉS⁵ 

¹Instituto de Investigación en Comunicación Óptica (IICO), Universidad Autónoma de San Luis Potosí, Av. Karakorum No. 1470 Lomas 4^a Secc., 78210, San Luis Potosí, Mexico

²Consejo Nacional de Ciencia y Tecnología (CONACYT), Av. Insurgentes Sur No. 1582, Col. Crédito Constructor, Del. Benito Juárez, México, 039040, D.F., Mexico

³Centro de Investigaciones en Óptica (CIO), Loma del Bosque No. 115, Col. Lomas del Campestre, 37150, León, Guanajuato, Mexico

⁴Instituto Nacional de Astrofísica, Óptica y Electrónica (INAOE), Luis Enrique Erro No 1, Departamento de Óptica, 72000 Puebla, Mexico

⁵Universidad de Valencia, Departamento de Física Aplicada y Electromagnetismo, ICMUV, c/Dr. Moliner 50, Burjassot, 46100 Valencia, Spain

*miguel.bello@uaslp.mx

Abstract: A tunable single- and dual-wavelength thulium-doped all-fiber laser is demonstrated based on the implementation of an in-fiber acousto-optic tunable bandpass filter (AOTBF). The AOTBF is fabricated to be operated in the 1.9 μm region, and takes advantage of the intermodal coupling effect produced by traveling flexural acoustic waves in an optical fiber. It exhibits a 3-dB bandwidth of 2.04 nm with an insertion loss of 4.75 dB. The tuning properties of the AO device allows a continuous-wave operation with characteristics of wide tuning range (211.5 nm), narrow linewidth (50 pm) and high signal-to-noise ratio (60 dB). In the dual-wavelength regime, the laser is capable of independent tuning of each of the laser lines, achieving a tunable dual-wavelength emission that extends from 1802.67 to 1932.75 nm. A controllable wavelength spacing with minimum and maximum separations of 1.04 and 130.08 nm is obtained.

© 2019 Optical Society of America under the terms of the [OSA Open Access Publishing Agreement](#)

1. Introduction

Dual-wavelength fiber lasers with characteristics of narrow linewidth, high stability and broadband tunability are very attractive optical sources with applications in many research fields such as THz radiation [1–3], coherent anti-Stokes Raman scattering [4], optical sensing [5] and high-speed communication systems [6], among others. Currently, and derived from the growing interest in developing all-fiber devices for the 2-micron wavelength region, various approaches of dual-wavelength thulium-doped fiber lasers (TDFLs) have been proposed and demonstrated based on the inclusion of different types of fiber-optic components, such as fiber Bragg gratings (FBGs) [7–9], Mach-Zehnder interferometers [10–12], tunable filters [12–14], and Sagnac loops [15–19], among others, all of them offering the advantages of high stability and easy implementation. Notwithstanding, from a practical point of view, most of these approaches require of arbitrary adjustments of polarization controllers (PCs) or variable optical attenuators (VOAs), which impose limitations in terms of repeatability and reliability. For these reasons, and despite the

Broadband tuning of a long-cavity all-fiber mode-locked thulium-doped fiber laser using an acousto-optic bandpass filter

E. HERNÁNDEZ-ESCOBAR,¹ M. BELLO-JIMÉNEZ,^{1,*} A. CAMARILLO-AVILÉS,¹ R. LÓPEZ-ESTOPIER,^{1,2} O. POTTIEZ,³ M. V. HERNÁNDEZ-ARRIAGA,⁴ M. DURÁN-SÁNCHEZ,^{2,5} B. IBARRA-ESCAMILLA,⁵ AND M. V. ANDRÉS⁶

¹Instituto de Investigación en Comunicación Óptica (IICO), Universidad Autónoma de San Luis Potosí, Av. Karakorum No. 1470 Lomas 4^a Secc., 78210 San Luis Potosí, Mexico

²Consejo Nacional de Ciencia y Tecnología (CONACYT), Av. Insurgentes Sur No. 1582, Col. Crédito Constructor, Del. Benito Juárez, México, D.F. 039040, Mexico

³Centro de Investigaciones en Óptica (CIO), Loma del Bosque No. 115, Col. Lomas del Campestre, León, Guanajuato 37150, Mexico

⁴Instituto Tecnológico Superior de Rioverde, Carretera Rioverde-San Ciró km. 4.5, 79610 Rioverde, San Luis Potosí, Mexico

⁵Instituto Nacional de Astrofísica, Óptica y Electrónica (INAOE), Luis Enrique Erro No 1, Departamento de Óptica, 72000 Puebla, Mexico

⁶Universidad de Valencia, Departamento de Física Aplicada y Electromagnetismo, ICMUV, c/Dr. Moliner 50, Burjassot, 46100 Valencia, Spain

*Corresponding author: miguel.bello@uaslp.mx

Received 31 May 2019; revised 24 July 2019; accepted 25 July 2019; posted 26 July 2019 (Doc. ID 368986); published 22 August 2019

A long-cavity passively mode-locked thulium-doped all-fiber laser is reported incorporating a tapered acousto-optic tunable bandpass filter (AOTBF). The operation of the AOTBF relies on the intermodal coupling between core and cladding modes when a flexural acoustic wave propagates along an 80 μm tapered fiber. The filter works in transmission and exhibits a 3 dB bandwidth of 9.02 nm with an insertion loss of 3.4 dB. The laser supports ultrashort pulse generation at a low repetition rate of 784.93 kHz. Optical pulses with 2.43 nm of optical bandwidth and 2.1 ps pulse duration were obtained in a broad tuning range from 1824.77 to 1905.16 nm. © 2019 Optical Society of America

<https://doi.org/10.1364/OL.44.004183>

Mode-locked fiber lasers (MLFLs) have received a great deal of attention in the past years because of their capability to generate short or ultrashort optical pulses featuring low repetition rates [1–7]. For applications that require ultrashort optical pulses and sub-megahertz repetition rates, one of the most common schemes relies on the use of pulse picker devices [8–11], but this method introduces significant losses and increases the laser complexity. For this reason, the development of long-cavity all-fiber approaches has emerged as an alternative solution to overcome these drawbacks.

In the framework of MLFLs, passive configurations possess the advantage of generating the shortest optical pulses, but in a long-cavity scheme—i.e., lasers with a cavity length from a few hundreds of meters to several kilometers—the generation of wave-breaking free optical pulses becomes a difficult task. Therefore, the development of all-fiber elements with capacity to provide a robust and stable laser performance is an issue of

particular interest. Following this research line, in-fiber acousto-optic (AO) devices based on flexural acoustic waves have been proposed and demonstrated as efficient bandpass filters that can work in transmission [12–15]. Among these approaches, our group has proposed an AO tunable bandpass filter (AOTBF) that uses a tiny section of coreless optical fiber as a core-mode blocker (CMB) [14,16,17], and generates no frequency shift. Now, and because of the growing interest in developing broad-bandwidth all-fiber devices, an improved AOTBF is presented based on the inclusion of a tapered optical fiber. The versatility of this AO device is demonstrated near the 2 μm region as a wavelength-selective element in a thulium-doped fiber laser (TDFL).

The bandpass characteristics of the AOTBF are analyzed after the inclusion of an 80 μm tapered optical fiber. Experimental results show a reasonably wide (56.29 nm) and deep (22.2 dB) attenuation notch for the CMB, and the tapered AOTBF exhibits a 3 dB bandpass transmission bandwidth of 9.02 nm. This result is at least 9 times broader than the one obtained with a nontapered fiber [14]. The filter capabilities are investigated in a long-cavity passively mode-locked TDFL, showing that ultrashort pulse generation is supported by our setup. These results, to the best of our knowledge, are the first results describing an in-fiber AO tunable bandpass filter that fulfills the requirements of broadband operation and stable single ultrashort pulse generation in a long-cavity fiber laser (repetition rate <1 MHz).

A schematic view of the AO tunable bandpass filter is shown in Fig. 1. A radio frequency (RF) source is used to drive a 20 mm piezoelectric disk (PD), and the acoustic vibrations are concentrated into an uncoated section of a tapered optical fiber through the tip of the aluminum horn. The section L of

Polarization mapping of a dual-wavelength passively mode-locked fiber ring laser

Y E Bracamontes-Rodríguez¹ , O Pottiez¹ , J P Lauterio Cruz^{1,2} ,
E García-Sánchez¹, J C Hernández-García^{2,3} , M Bello-Jiménez⁴ ,
B Ibarra-Escamilla⁵  and E A Kuzin⁵ 

¹Centro de Investigaciones en Óptica, Lomas del Bosque 115, Col. Lomas del Campestre, León, Gto. 37150, México

²Departamento de Electrónica, División de Ingenierías CIS, Universidad de Guanajuato, Carretera Salamanca-Valle de Santiago Km 3.5 + 1.8 Km, Comunidad de Palo Blanco, Salamanca, Gto. 36885, México

³Consejo Nacional de Ciencia y Tecnología, Av. Insurgentes Sur No. 1582, Col. Crédito Constructor, Del. Benito Juárez, C.P. 039040, México

⁴Instituto de investigación en Comunicación Óptica (IICO), Universidad Autónoma de San Luis Potosí, Av. Karakorum No. 1470 Lomas 4aSecc., 78210 San Luis Potosí, México

⁵Instituto Nacional de Astrofísica, Óptica y Electrónica, L.E. Erro 1, Sta. Ma. Tonantzintla, Pue. 72824, Mexico

E-mail: yazminbr@cio.mx

Received 8 October 2018, revised 22 January 2019

Accepted for publication 1 March 2019

Published 19 March 2019



CrossMark

Abstract

We report an extensive experimental study of a dual-wavelength (1530 and 1560 nm) passively mode-locked fiber laser in a ring configuration with strict control of the polarization state. Different types of laser operation are identified, which are classified into ten mode locking regimes (solitons-noise-like pulsing, solitons-solitons, solitons-CW, bound solitons-CW, solitons (1530 nm), CW-solitons, CW-bound solitons, Q-switched-like noise-like pulsing, steady noise-like pulsing at 1530 nm and intermittent mode locking), which are mapped in terms of the polarization settings (ellipticity and azimuth). The resulting map establishes, in a clear and repeatable way, the relation existing between each mode locking regime and the polarization adjustment, which allows controlling at the same time intracavity losses, the gain profile, the cavity spectral transfer function, as well as the nonlinear switching characteristic.

Keywords: lasers erbium, lasers ring, mode-locked lasers, nonlinear optics, fibers, polarization

(Some figures may appear in colour only in the online journal)

1. Introduction

Passively mode-locked fiber lasers are flexible sources that are capable of producing a wide variety of optical pulses, such as conservative solitons, dispersion-managed solitons, similaritons [1], and a broad variety of dissipative solitons [2], which include, among others, dissipative soliton resonance [3] and spiny solitons [4]. One single or multiple solitons can appear in the cavity [5]. Multiple solitons can distribute randomly or equidistantly along the cavity (harmonic mode locking) [6], and form pairs of bound solitons [7–9], soliton molecules or crystals [10]. They can present arrangements

that recall states of matter (soliton gas, liquid, plasma, etc) [11], display complex dynamics, such as the soliton rain [12], or be subject to chaotic relative motion, in which case, their frequent interactions can lead to extreme-intensity events (optical rogue waves) [13]. Complex polarization dynamics of solitons have also been evidenced in passively mode-locked fiber lasers [8, 14]. Alternatively, these sources can operate in a distinctive regime, in which complex bursts of radiation, known as noise-like pulses (NLPs), are generated [15–19]. In this frame, connections with optical rogue waves [20–23] and a wide range of complex behaviors have also been identified [24–28].

ON THE NUMBER OF UNKNOT DIAGRAMS*

CAROLINA MEDINA[†], JORGE RAMÍREZ-ALFONSÍN[‡], AND GELASIO SALAZAR[§]

Abstract. Let D be a knot diagram, and let \mathcal{D} denote the set of diagrams that can be obtained from D by crossing exchanges. If D has n crossings, then \mathcal{D} consists of 2^n diagrams. A folklore argument shows that at least one of these 2^n diagrams is unknot, from which it follows that every diagram has finite unknotting number. It is easy to see that this argument can be used to show that actually \mathcal{D} has more than one unknot diagram, but it cannot yield more than $4n$ unknot diagrams. We improve this linear bound to a superpolynomial bound by showing that at least $2^{\sqrt[3]{n}}$ of the diagrams in \mathcal{D} are unknot. We also show that either all the diagrams in \mathcal{D} are unknot or there is a diagram in \mathcal{D} that is a diagram of the trefoil knot.

Key words. knot shadows, knot diagrams, unknot diagrams, plane curves

AMS subject classifications. 57M25, 05C10, 57M15

DOI. 10.1137/17M115462X

1. Introduction. We follow standard knot theory terminology as in [1]. All knots under consideration are tame, that is, they have regular diagrams. All diagrams under consideration are regular.

1.1. Our main result. A staple in every elementary knot theory course is that, given any diagram D , it is always possible to turn D into a diagram of the unknot (that is, into an *unknot diagram*) by performing some crossing exchanges on D (see Figure 1). The minimum number of such crossing exchanges that turn D into an unknot diagram is a well-studied parameter, the *unknotting number* of D .

We review in section 2 the well-known argument that turns any diagram D into an unknot diagram by performing crossing exchanges. As we shall remark, this argument actually produces more than one unknot diagram from D , but it gives a relatively small number: if D has n crossings, this idea yields at most $4n$ distinct unknot diagrams that can be obtained from D by crossing exchanges. Our main result is that actually there is always a superpolynomial number of such unknot diagrams.

THEOREM 1. *Let D be a knot diagram with n crossings. Then there are at least $2^{\sqrt[3]{n}}$ distinct unknot diagrams that can be obtained by performing crossing exchanges on D .*

As far as we know, no nontrivial general lower bound along the lines of Theorem 1 has been previously reported. There is, however, a substantial amount of work related to the complementary problem: out of the 2^n diagrams that can be obtained from

*Received by the editors October 30, 2017; accepted for publication (in revised form) December 17, 2018; published electronically February 5, 2019.

<http://www.siam.org/journals/sidma/33-1/M115462.html>

Funding: This work started while the second author visited the other authors, supported by the Laboratorio Internacional Asociado Solomon Lefschetz (LAISLA), which has now become the Unité Mixte Internationale CNRS-CONACYT-UNAM “Laboratoire Solomon Lefschetz.” The first author was supported by Fordecyt grant 265667, the second author was partially supported by PICS07848 grant, and the third author was supported by Conacyt grant 222667 and by FRC-UASLP.

[†]Instituto de Física, UASLP, San Luis Potosí, Mexico, 78000 (cmedina@ifisica.uaslp.mx).

[‡]IMAG, Univ. Montpellier, CNRS, 34095 Montpellier, France (jorge.ramirez-alfonsin@umontpellier.fr).

[§]Unité Mixte Internationale CNRS-CONACYT-UNAM “Laboratoire Solomon Lefschetz,” Cuernavaca, Mexico (gsalazar@ifisica.uaslp.mx).



The knots that lie above all shadows [☆]

Carolina Medina ^a, Gelasio Salazar ^{b,*}

^a Department of Mathematics, University of California, Davis, CA 95616, USA

^b Instituto de Física, Universidad Autónoma de San Luis Potosí, SLP 78000, Mexico



ARTICLE INFO

Article history:

Received 28 June 2019

Accepted 18 October 2019

Available online 23 October 2019

MSC:

primary 57M25

Keywords:

Knots

Knot projections

Knot shadows

Knot diagrams

ABSTRACT

We show that for each even integer $m \geq 2$, every reduced shadow with sufficiently many crossings is a shadow of a torus knot $T_{2,m+1}$, or of a twist knot T_m , or of a connected sum of m trefoil knots.

© 2019 Elsevier B.V. All rights reserved.

1. Introduction

A *shadow* is an orthogonal projection of a knot onto a plane. The *size* of a shadow is its number of crossings. As usual, all shadows under consideration are *regular*, that is, they have no triple points and no points of self-tangency. A shadow S *resolves into* a knot K if there is an over/under assignment at the crossings of S that gives a diagram of K .

This work revolves around the following fundamental problem.

Question 1.1. Given a shadow S , which knots K satisfy that S resolves into K ?

To investigate this question we must restrict our attention to *reduced* shadows, that is, shadows with no nugatory crossings. As in [6], we say that a crossing x in a shadow S is *nugatory* if $S \setminus \{x\}$ is disconnected. This restriction is crucial: it is easy to exhibit arbitrarily large non-reduced shadows that only resolve into the unknot.

[☆] The first author was supported by Fordecyt grant 265667, and is currently supported by a Fulbright Visiting Scholar Grant at UC Davis. The second author was supported by Conacyt grant 222667 and by FRC-UASLP.

* Corresponding author.

E-mail addresses: cmolina@math.ucdavis.edu (C. Medina), gsalazar@ifisica.uaslp.mx (G. Salazar).



Contents lists available at ScienceDirect

Journal of Combinatorial Theory,
Series Bwww.elsevier.com/locate/jctb

Toroidal grid minors and stretch in embedded graphs

Markus Chimani^{a,1}, Petr Hliněný^{b,2}, Gelasio Salazar^{c,3}^a Faculty of Mathematics/Computer Science, Osnabrück University, Osnabrück, Germany^b Faculty of Informatics, Masaryk University, Brno, Czech Republic^c Instituto de Física, Universidad Autónoma de San Luis Potosí, San Luis Potosí, Mexico

ARTICLE INFO

Article history:

Received 4 March 2014

Available online xxx

Keywords:

Graph embeddings

Compact surfaces

Edge-width

Toroidal grid

Crossing number

Stretch

ABSTRACT

We investigate the *toroidal expanse* of an embedded graph G , that is, the size of the largest toroidal grid contained in G as a minor. In the course of this work we introduce a new embedding density parameter, the *stretch* of an embedded graph G , and use it to bound the toroidal expanse from above and from below within a constant factor depending only on the genus and the maximum degree. We also show that these parameters are tightly related to the planar *crossing number* of G . As a consequence of our bounds, we derive an efficient constant factor approximation algorithm for the toroidal expanse and for the crossing number of a surface-embedded graph with bounded maximum degree.

© 2019 Elsevier Inc. All rights reserved.

E-mail addresses: markus.chimani@uni-osnabrueck.de (M. Chimani), hlineny@fi.muni.cz (P. Hliněný), gelasio.salazar@gmail.com (G. Salazar).

¹ Supported by the German Research Foundation (DFG), projects CH 897/2-1 and CH 897/2-2.² Supported by the Czech Science Foundation, projects 14-03501S (until 2016) and 17-00837S.³ Supported by CONACYT Grant 106432.<https://doi.org/10.1016/j.jctb.2019.05.009>

0095-8956/© 2019 Elsevier Inc. All rights reserved.

THE UNAVOIDABLE ARRANGEMENTS OF PSEUDOCIRCLES

CAROLINA MEDINA, JORGE RAMÍREZ-ALFONSÍN, AND GELASIO SALAZAR

(Communicated by Patricia L. Hersh)

ABSTRACT. A fact closely related to the classical Erdős-Szekeres theorem is that cyclic arrangements are the only *unavoidable* simple arrangements of pseudolines: for each fixed $m \geq 1$, every sufficiently large simple arrangement of pseudolines has a cyclic subarrangement of size m . In the same spirit, we show that there are three unavoidable arrangements of pseudocircles.

1. INTRODUCTION

A seminal result by Erdős and Szekeres [3] states that for every fixed integer $k \geq 3$, every sufficiently large set of points in general position in \mathbb{R}^2 contains k points in *convex position*, that is, k points that are the vertices of a convex k -gon. In the dual setting, a set (or *arrangement*) of lines in \mathbb{R}^2 is *in general position* if no two are parallel, and no three lines intersect at a common point. An arrangement of k lines is in *convex position* if one of its cells is bounded by a k -gon, which necessarily contains a segment from each of the k lines. The dual version of the Erdős-Szekeres theorem for lines is that for every fixed $k \geq 3$, every sufficiently large arrangement of lines in general position contains k lines in convex position (see [1]).

It must be noted that the point and line versions of the Erdős-Szekeres theorem are not dual to each other in \mathbb{R}^2 , but they are so in the projective plane \mathbb{RP}^2 . A *pseudoline* is a noncontractible simple closed curve in \mathbb{RP}^2 . An *arrangement of pseudolines* is a set of pseudolines that cross each other exactly once. An arrangement of pseudolines is *simple* if no three pseudolines have a common point. Two arrangements of pseudolines are *isomorphic* if the cell complexes they induce in \mathbb{RP}^2 are isomorphic.

A simple arrangement of pseudolines is *cyclic* if its pseudolines can be labelled $1, 2, \dots, m$, so that each pseudoline $i \in [m]$ intersects the pseudolines in $\{1, 2, \dots, m\} \setminus \{i\}$ in increasing order (see Figure 1). Cyclic arrangements of pseudolines have a cell whose boundary contains a segment from each pseudoline, and so they are the natural counterpart in \mathbb{RP}^2 to arrangements of lines in convex position in \mathbb{R}^2 .

The following statement is the version of the Erdős-Szekeres theorem for simple arrangements of pseudolines. In the spirit of [15], this shows that cyclic arrangements are the only *unavoidable* arrangements of pseudolines.

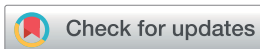
Received by the editors August 18, 2018, and, in revised form, October 19, 2018.

2010 *Mathematics Subject Classification*. Primary 52C30; Secondary 05C10, 52C40.

The first author was supported by Fordecyt grant 265667.

The second author was partially supported by PICS07848 grant and by Program MATH-SUD 41327ZL - FLanASAGraTA.

The third author was supported by Conacyt grant 222667 and by FRC-UASLP.



Cite this: *RSC Adv.*, 2019, 9, 13677

Thermodynamic, structural and dynamic properties of ionic liquids [C₄mim][CF₃COO], [C₄mim][Br] in the condensed phase, using molecular simulations†

Joel Sánchez-Badillo,^a Marco Gallo,^b Ricardo A. Guirado-López^c and Jorge López-Lemus^d

In this work a series of thermodynamic, structural, and dynamical properties for the 1-butyl-3-methylimidazolium trifluoroacetate ([C₄mim][CF₃COO]) and 1-butyl-3-methylimidazolium bromide ([C₄mim][Br]) ionic liquids (ILs) were calculated using Non-polarizable Force Fields (FF), parameterized using a methodology developed previously within the research group, for condensed phase applications. Properties such as the Vapor-Liquid Equilibrium (VLE) curve, critical points (ρ_c , T_c), Radial, Spatial and Combined Distribution Functions and self-diffusion coefficients were calculated using Equilibrium Molecular Dynamics simulations (EMD); other properties such as shear viscosities and thermal conductivities were calculated using Non-Equilibrium Molecular Dynamics simulations (NEMD). The results obtained in this work indicated that the calculated critical points are comparable with those available in the literature. The calculated structural information for these two ILs indicated that the anions interact mainly with hydrogen atoms from both the imidazolium ring and the methyl chain; the bromide anion displays twice the hydrogen coordination number than the oxygen atoms from the trifluoroacetate anion. Furthermore, Non-Covalent interactions (NCI index), determined by DFT calculations, revealed that some hydrogen bonds in the [C₄mim][Br] IL displayed similar strength to those in the [C₄mim][CF₃COO] IL, in spite of the shorter O⁻-H distances found in the latter IL. The majority of the calculated transport properties presented reasonable agreement with the experimental available data. Nonetheless, the self-diffusion coefficients determined in this work are under-estimated with respect to experimental values; however, by escalating the electrostatic atomic charges for the anion and cation to $\pm 0.8e$, only for this property, a remarkable improvement was obtained. Experimental evidence was recovered for most of the calculated properties and to the best of our knowledge, some new predictions were done mainly in thermodynamic states where data are not available. To validate the FF, developed previously within the research group, dynamic properties were also evaluated for a series of ILs such as [C₄mim][PF₆], [C₄mim][BF₄], [C₄mim][OMs], and [C₄mim][NTf₂] ILs.

Received 18th March 2019

Accepted 23rd April 2019

DOI: 10.1039/c9ra02058f

rsc.li/rsc-advances

Introduction

Ionic liquids (ILs) are molten salts composed of only cations and anions in a liquid state at temperatures below 100 °C.¹ In the last two decades these substances have attracted great interest because of their physicochemical properties such as low vapor pressure, thermal stability, decomposition at high

temperatures, isothermal compressibilities similar to water, large electrochemical windows, wide range of shear viscosities, and suitability for applications as extracting agents, heat transfer fluids, electrolytes for batteries, lubricants, and catalysts.²⁻⁶ ILs are considered as a green alternative for the replacement of Volatile Organic Compounds (VOCs) in many industrial processes without the necessity of major changes in the main flow sheet and equipment.⁷

It is known that by combining different cations and anions, it is possible to design ILs with specific properties for well-defined applications.⁸ Nevertheless, the experimental search for specific ILs can be an expensive and a time consuming task, therefore different economical alternatives need to be employed such as computer simulations. Molecular Dynamics simulations can describe molecular and atomic interactions to predict and evaluate a wide range of physicochemical properties of ILs. This allows the design of new solvents with unique

^aFacultad de Ciencias Químicas, Universidad Autónoma de San Luis Potosí, Zona Universitaria, Av. Manuel Nava No. 6, San Luis Potosí, C.P. 78210, Mexico

^bTecnológico Nacional de México/ITCJ, Av. Tecnológico No. 1340, Cd. Juárez, Chihuahua, C.P. 32500, Mexico. E-mail: mgallo@itcj.edu.mx

^cInstituto de Física "Manuel Sandoval Vallarta", Universidad Autónoma de San Luis Potosí, Alvaro Obregón No. 64, San Luis Potosí, C.P. 78000, Mexico

^dFacultad de Ciencias, Universidad Autónoma del Estado de México, Toluca, Estado de México, C.P. 50000, Mexico

† Electronic supplementary information (ESI) available. See DOI: 10.1039/c9ra02058f





Counting Hamiltonian Cycles in the Matroid Basis Graph

Cristina G. Fernandes¹ · César Hernández-Vélez² · José C. de Pina¹ · Jorge Luis Ramírez Alfonsín³

Received: 9 January 2018 / Revised: 3 January 2019 / Published online: 9 February 2019
© Springer Japan KK, part of Springer Nature 2019

Abstract

We present superfactorial and exponential lower bounds on the number of Hamiltonian cycles passing through any edge of the basis graph of generalized Catalan, uniform, and graphic matroids. All lower bounds were obtained by a common general strategy based on counting appropriated cycles of length four in the corresponding matroid basis graph.

Keywords Matroid basis graph · Generalized Catalan matroid · Hamiltonian cycle

Mathematics Subject Classification 05B35 · 05C38 · 05C45

1 Introduction

Basis graphs of matroids have been extensively studied. Gel'fand and Serganova [11] proved that basis graphs are 1-skeletons of basis polytopes [6,7]. Maurer [15] gave a characterization of basis graphs, Liu [12–14] investigated their connectivity, and Donald, Holzmann, and Tobey [9] gave a characterization of basis graphs of uniform matroids.

✉ César Hernández-Vélez
cesar.velez@uaslp.mx

Cristina G. Fernandes
cris@ime.usp.br

José C. de Pina
coelho@ime.usp.br

Jorge Luis Ramírez Alfonsín
jorge.ramirez-alfonsin@umontpellier.fr

¹ Instituto de Matemática e Estatística, Universidade de São Paulo, São Paulo, Brazil

² Facultad de Ciencias, Universidad Autónoma de San Luis Potosí, San Luis Potosí, México

³ IMAG, Univ. Montpellier, CNRS, Montpellier, France



Construction of a power electronic source for cold plasma generation

Construcción de una fuente de electrónica de potencia para generación de plasma frío

Martínez-Montejano Roberto Carlos

Unidad Académica Multidisciplinaria Zona Media

Universidad Autónoma de San Luis Potosí

Correo: roberto.montejano@uaslp.mx

<https://orcid.org/0000-0002-8996-4134>

Castillo-Escandón Carlos Miguel

Unidad Académica Multidisciplinaria Zona Media

Universidad Autónoma de San Luis Potosí

Correo: miguel213211@yahoo.com

<https://orcid.org/0000-0001-6739-9405>

Espinoza-López Víctor Esteban

Unidad Académica Multidisciplinaria Zona Media

Universidad Autónoma de San Luis Potosí

Correo: victor.espinoza@uaslp.mx

<https://orcid.org/0000-0001-8808-2319>

Campos-Cantón Isaac

Universidad Autónoma de San Luis Potosí

Facultad de Ciencias

Correo: icampos@fciencias.uaslp.mx

<https://orcid.org/0000-0002-3189-3417>

Neira-Velázquez María Guadalupe

Departamento de Síntesis de Polímeros

Centro de Investigación en Química Aplicada

Correo: guadalupe.neira@ciqa.edu.mx

<https://orcid.org/0000-0002-3850-850X>

Soria-Arguello Gustavo

Departamento de Síntesis de Polímeros

Centro de Investigación en Química Aplicada

Correo: gustavo.soria@ciqa.edu.mx

<https://orcid.org/0000-0002-9771-8638>

Abstract

This paper presents the development of a high voltage and high-frequency power electronics source, for plasma generation, at atmospheric pressure and vacuum, using helium and air as working gases. The source design consists of an inductive (L) full bridge series resonant inverter at high frequency, where the control implemented allows varying duty cycle and frequency. Plasma generation is made by high voltage with the power signal applied on two electrodes, which provides a strong electric field that excites, and thus, ionize helium particles or air particles. The power electronic source operation was tested in different plasma reactor configurations (dielectric barrier discharge, double dielectric barrier discharge, and jet type discharge). The developed power electronics source shows a correct performance and generate a strong electric field to achieve the plasma discharges desired.

Keywords: High voltage power source, cold plasma, resonant full bridge inverter.

Resumen

Este artículo presenta el desarrollo de una fuente de electrónica de potencia de alto voltaje y alta frecuencia para la generación de plasma al vacío y a presión atmosférica, utilizando helio y aire como gases precursores. El diseño de la fuente consiste en un inversor de resonante en serie de puente completo con carga inductiva (L), que tiene un control implementado que permite variar el ciclo de trabajo y la frecuencia. La generación del plasma se logra aplicando una señal de alto voltaje en dos electrodos, que proveen un campo eléctrico fuerte que excita e ioniza partículas de helio o aire. Las descargas de plasma fueron hechas en diferentes configuraciones de electrodos: descarga de barrera dieléctrica, descarga de doble barrera dieléctrica y descarga tipo jet. La fuente de electrónica de potencia desarrollada demuestra su capacidad de desarrollar el campo eléctrico lo suficientemente fuerte para alcanzar las descargas de plasma deseadas.

Descriptores: Fuente de potencia de alto voltaje, plasma frío, inversor resonante de puente completo.



Cite this: *Phys. Chem. Chem. Phys.*,
2019, **21**, 24077

Nanotubols under H₂O₂ exposure: is it possible to poly-hydroxylate carbon nanotubes?†

J. Vicente-Santiago,^{‡,a} J. Cornejo-Jacob,^{‡,a} D. Valdez-Pérez,^b J. Ruiz-García^b and R. A. Guirado-López^{b,*a}

We present a combined experimental and theoretical study dedicated to analyze the variations in the surface chemistry of hydroxylated multiwalled carbon nanotubes (MWCNTs), so called nanotubols, when exposed to H₂O₂ at high temperatures. The formation, surface density, and distribution of oxygen-containing functional groups are studied by infrared (IR) and X-ray photoelectron spectroscopy (XPS), as well as density functional theory (DFT) calculations performed on model functionalized carbon nanotubes (CNTs). After H₂O₂ exposure, the initial composition of –OH, –C=O, and –COOH substituents notably changes, with carbonyl –C=O groups being the ones that show the most notable increase on the carbon surface. Our highly oxidized MWCNTs are partially soluble and form complex two-dimensional patterns at the air–water interface, as evidenced by Brewster angle microscopy. In a second step, these films can be transferred to solid substrates to form porous multilayered carbon nanostructures with complex morphologies. In particular, and for the first time, we report the synthesis of “stadium-like” configurations made of MWCNT units whose formation and stability are a direct consequence of the self-assembly process occurring at the air/water interface. DFT calculations suggest the formation of molecular islands of oxygen-containing functional groups on the CNT surface. In addition, nudged elastic band studies reveal that, for these adsorbed phases, the reaction between two neighboring OH groups to produce atomic oxygen and a physisorbed water molecule is characterized by energy barriers of ~0.2 eV. These small values could be at the origin of the sizable increase in chemisorbed single-oxygen species determined by XPS data after H₂O₂ treatment at 60 °C. The simulation of the C 1s binding energies (BE) allows us to more clearly identify the different oxygen-containing functionalities as well as to reveal how the local atomic environment affects their characteristic BEs. Even if we were unable to polyhydroxylate our carbon nanotubes, we believe that H₂O₂-treated MWCNTs are interesting materials for more complex post-functionalization procedures that might lead to the fabrication of novel carbon nanostructures.

Received 4th June 2019,
Accepted 10th October 2019

DOI: 10.1039/c9cp03148k

rsc.li/pccp

1. Introduction

In the last few years, it has been clearly established that the functionalization of the external surface of single walled and multi-walled carbon nanotubes (MWCNTs) can lead to strong variations in their electronic, chemical, and transport properties, as well as to notable changes in their interaction with the

surrounding media (see ref. 1 and references therein). We can distinguish two general strategies to achieve the surface modification of carbon nanotubes (CNTs), namely, non-covalent^{2–6} and covalent^{7–11} functionalization. While the former allows the synthesis of weakly interacting CNT–molecule complexes, the latter leads to highly stable compounds. In particular, the addition of oxygen-containing functional groups is the most common surface modification, being easily achieved for example by performing H₂SO₄/HNO₃^{12,13} as well as Na₂ZnO₂, NaAlO₂, and NaOH treatments¹⁴ on pristine CNTs at high temperatures. Infrared (IR) and X-ray photoelectron spectroscopy (XPS) experiments on these samples reveal the existence of carbonyl, carboxylic, and hydroxyl groups, with hydroxyl groups being the most abundant species on the nanotube surface.^{12–16}

The existence of chemisorbed –C=O, –COOH, and –OH substituents on CNTs leads to a better dispersion of CNTs in polymer matrices¹⁷ and, most importantly, these chemical

^a Instituto de Física “Manuel Sandoval Vallarta”, Universidad Autónoma de San Luis Potosí, Álvaro Obregón 64, San Luis Potosí, S.L.P., 78000, Mexico.
E-mail: guirado@ifisica.uaslp.mx

^b Instituto Politécnico Nacional, UPALM, Edif. Z-4 3er Piso, CP 07738, México CDMX, México

† Electronic supplementary information (ESI) available: Low-energy atomic configurations for hydroxyl groups chemisorbed on C₆₀. Calculated energy barriers ΔE for the OH + OH → O + H₂O reaction on the C₆₀ fullerene. See DOI: 10.1039/c9cp03148k

‡ These authors contributed equally to this work.



An algorithm for the *in situ* analysis of optical reflectance anisotropy spectra

J. Ortega-Gallegos^{a,*}, A. Lastras-Martínez^{a,*}, L.E. Guevara-Macías^a, J.G. Santiago García^a,
D. Ariza-Flores^{a,b}, R. Castro-García^{a,b}, R.E. López-Estopier^{a,b}, R.E. Balderas-Navarro^a,
L.F. Lastras-Martínez^a



^a Instituto de Investigación en Comunicación Óptica, Universidad Autónoma de San Luis Potosí, Alvaro Obregón 64, San Luis Potosí, SLP 78000, Mexico

^b CONACyT - Instituto de Investigación en Comunicación Óptica, Universidad Autónoma de San Luis Potosí, Alvaro Obregón 64, San Luis Potosí, SLP 78000, Mexico

ARTICLE INFO

Communicated by R.M. Biefeld

Keywords:

A1. Characterization
A1. Growth models
A1. Surface processes
A3. Molecular beam epitaxy
B2. Semiconducting gallium arsenide
B2. Semiconducting III-V materials

ABSTRACT

We report on a computer algorithm for the *in situ* analysis of reflectance anisotropy (RA) spectra in a time frame compatible with the epitaxial growth of cubic semiconductors. This algorithm allows for the *in situ* acquisition of RA spectra and their decomposition into two components whose amplitude depends on the As coverage of the semiconductor surface. One of such components is associated with the surface orthorhombic strain due to the surface reconstruction and has an amplitude that strongly depends with surface reconstruction and thus As coverage. This fact opens the possibility of using reflectance anisotropy spectroscopy (RAS) as an optical probe to characterize the As surface coverage in real time. To demonstrate the performance of the algorithm we report on RA measurements carried out during the homoepitaxial growth of GaAs (001). We show that the algorithm is capable of analyzing a set of 500 RA spectra in a time span of about 10 s. This allows for a range of applications for the developed algorithm, including the surface characterization and fine tuning of the substrate stoichiometry just before epitaxial growth, during the growth of the buffer layer.

1. Introduction

The growing complexity of advanced optoelectronic devices based on III-V semiconductors [1–3] demands probes for real-time growth monitoring with sub monolayer resolution. Non-invasive optical probes, such as reflectance anisotropy spectroscopy (RAS), are advantageous for this application given their high sensitivity, instrumental simplicity and fast response [4–6]. RAS is an optical polarization contrast technique, based on the measurements of difference of reflectivity for two orthogonal polarized light beams [8]. This spectroscopy enhances the surface related response by taking advantage of the reduced symmetry of the surface region of a cubic crystal. We note that for polarizations of the incident beam parallel to the principal axes of the crystal, the signal arising from the isotropic bulk is suppressed [4,5,9,10].

The usefulness of RAS as a surface characterization technique stems from the strong dependence of the reflectance anisotropy (RA) line shape on surface reconstruction [4–7]. In this respect, GaAs surfaces with reconstructions $c(4 \times 4)$ and (2×4) show characteristic and well differentiated RA lineshapes. However, despite the fact that the surface specificity of anisotropic reflectance has been recognized for a long time [11], the development of the full potential of the technique for the

real-time characterization of epitaxial growth has been traditionally hampered by the lack of anisotropic reflectance spectrometers with high enough, both, spectrum acquisition speed and spectral resolution.

Recently, we developed a rapid RA 32-channel spectrometer with the capability to measure in real-time fractional changes of monolayer coverage during epitaxial growth [12]. Taking advantage of such instrument, we carried out a series of real-time RAS measurements during the homoepitaxial growth of GaAs (001) under several As_4 overpressures and found that upon starting growth on an As-rich surface ($c(4 \times 4)$ reconstruction), the RAS amplitude undergoes a fast transient towards a less As-rich surface ((2×4) reconstruction). This transient is a function of both As overpressure and substrate temperature and takes place within the first monolayer (ML) growth period.

RA line shapes are, nevertheless, complex and not readily interpreted. Indeed, previously we have shown that the reflectance anisotropy (RA) spectra of both $c(4 \times 4)$ and (2×4) surfaces comprise two spectral components whose relative amplitude is a function of surface As coverage [13]. A first component is associated with the orthorhombic strain induced by surface reconstruction and its amplitude changes sign when shifting from $c(4 \times 4)$ to (2×4) reconstruction [13]. A second component shows an amplitude variation with no change of sign [16]. Additionally, it is noted that the RAS oscillations are mainly

* Corresponding authors.

E-mail addresses: jortega@cactus.iico.uaslp.mx (J. Ortega-Gallegos), alm@cactus.iico.uaslp.mx (A. Lastras-Martínez).

<https://doi.org/10.1016/j.jcrysgr.2019.03.002>

Received 15 November 2018; Received in revised form 5 February 2019; Accepted 1 March 2019

Available online 02 March 2019

0022-0248/ © 2019 Elsevier B.V. All rights reserved.

Differential reflectance contrast technique in near field limit: Application to graphene

Cite as: AIP Advances 9, 045309 (2019); <https://doi.org/10.1063/1.5092339>

Submitted: 10 February 2019 . Accepted: 29 March 2019 . Published Online: 10 April 2019

L. F. Lastras-Martínez , D. Medina-Escobedo, G. Flores-Rangel, R. E. Balderas-Navarro, O. Ruiz-Cigarrillo, R. Castro-García , M. del P. Morales-Morelos, J. Ortega-Gallegos, and M. Losurdo



View Online



Export Citations



CrossMark

ARTICLES YOU MAY BE INTERESTED IN

[Optical detection of graphene nanoribbons synthesized on stepped SiC surfaces](#)

Journal of Applied Physics **122**, 035701 (2017); <https://doi.org/10.1063/1.4993453>

[Note: A simple multi-channel optical system for modulation spectroscopies](#)

Review of Scientific Instruments **88**, 126107 (2017); <https://doi.org/10.1063/1.4998596>

[Rapid reflectance difference microscopy based on liquid crystal variable retarder](#)

Journal of Vacuum Science & Technology B **37**, 050604 (2019); <https://doi.org/10.1116/1.5122694>

AVS Quantum Science

Co-Published by



RECEIVE THE LATEST UPDATES





Prediction of epileptic seizures with convolutional neural networks and functional near-infrared spectroscopy signals



Roberto Rosas-Romero^{a,*}, Edgar Guevara^b, Ke Peng^c, Dang Khoa Nguyen^d, Frédéric Lesage^{c,e}, Philippe Pouliot^{c,e}, Wassim-Enrique Lima-Saad^a

^a Universidad de las Américas-Puebla, Mexico

^b CONACYT - Universidad Autónoma de San Luis Potosí, Mexico

^c École Polytechnique de Montréal, Canada

^d Hôpital Notre-Dame du CHUM, Canada

^e Montreal Heart Institute, Canada

ARTICLE INFO

Keywords:

Convolutional neural network (CNN)
Epileptic seizure prediction
Functional near-infrared spectroscopy (fNIRS)
Gradient descent method

ABSTRACT

There have been different efforts to predict epileptic seizures and most of them are based on the analysis of electroencephalography (EEG) signals; however, recent publications have suggested that functional Near-Infrared Spectroscopy (fNIRS), a relatively new technique, could be used to predict seizures. The objectives of this research are to show that the application of fNIRS to epileptic seizure detection yields results that are superior to those based on EEG and to demonstrate that the application of deep learning to this problem is suitable given the nature of fNIRS recordings. A Convolutional Neural Network (CNN) is applied to the prediction of epileptic seizures from fNIRS signals, an optical modality for recording brain waves. The implementation of the proposed method is presented in this work. Application of CNN to fNIRS recordings showed an accuracy ranging between 96.9% and 100%, sensitivity between 95.24% and 100%, specificity between 98.57% and 100%, a positive predictive value between 98.52% and 100%, and a negative predictive value between 95.39% and 100%. The most important aspect of this research is the combination of fNIRS signals with the particular CNN algorithm. The fNIRS modality has not been used in epileptic seizure prediction. A CNN is suitable for this application because fNIRS recordings are high dimensional data and they can be modeled as three-dimensional tensors for classification.

1. Introduction

Prediction of epileptic seizures refers to the analysis of brain signals, extracted from an epileptic patient, to detect the future occurrence of a seizure. There are four states within a brain signal, which is extracted from an epileptic patient. The *ictal* state is the signal fragment where an epileptic seizure occurs; the *pre-ictal* state is the segment that happens before the onset of a seizure; *post-ictal* is the state that follows a seizure, and *inter-ictal* is the fragment between the end of post-ictal and the start of pre-ictal. In this work, we merge post-ictal and inter-ictal states into one state, inter-ictal. Furthermore, we discard the ictal state since detecting an epileptic seizure, when it is happening, is of no interest for seizure prediction. Thus, we only consider two states, inter-ictal and pre-ictal. Epileptic seizure prediction is achieved when the system detects the pre-ictal state [1]. Real-time epileptic seizure prediction mainly consists of two stages: (1) extraction of a tensor from the signal of

interest, at any time position; and (2) classification of the tensor as inter-ictal or pre-ictal. Epileptic seizures are predicted when pre-ictal segments are correctly detected. Detection of the ictal state is of no interest since the goal is detecting a seizure before it happens by identifying the occurrence of the pre-ictal state. Thus, ictal fragments are of no use. There have been different efforts to predict seizures and most of them are based on the analysis of *electroencephalography* (EEG) signals [2]; however, recent publications have suggested that fNIRS signals, a relatively new modality, could be used to predict seizures [3,4]. fNIRS (*functional near-infrared spectroscopy*) is an optical technique, which conveys monitoring information about brain activity [5]; specifically, two physiological parameters or measurements, the relative level of *oxygenated hemoglobin* (HbO) and the relative level of *deoxygenated hemoglobin* (HbR). fNIRS signals are generated by injecting infrared lights of different wavelengths (650 nm–1000 nm) into the scalp, followed by registration of reflected light through optodes. Blood

* Corresponding author.

E-mail address: roberto.rosas@udlap.mx (R. Rosas-Romero).



Prolonged release of metformin by SiO₂ nanoparticles pellets for type II diabetes control



Rosalba Patiño-Herrera^{a,*}, José Francisco Louvier-Hernández^a, Eleazar M. Escamilla-Silva^a, Julie Chaumel^b, Alma Gabriela Palestino Escobedo^b, Elías Pérez^c

^a Departamento de Ingeniería Química, Tecnológico Nacional de México/Instituto Tecnológico de Celaya, Av. Tecnológico y Antonio García Cubas No. 600 Pte., Celaya, Guanajuato 38010, Mexico

^b Facultad de Ingeniería Química, UASLP, Álvaro Obregón 64, San Luis Potosí, S.L.P. 78000, Mexico

^c Instituto de Física, UASLP, Álvaro Obregón 64, San Luis Potosí, S.L.P. 78000, Mexico

ARTICLE INFO

Keywords:

Mesoporous silica nanoparticles
Metformin
Pellet
Drug delivery system
Drug release
Diabetes mellitus

ABSTRACT

Mesoporous silica nanoparticles (MSNPs) were synthesized and loaded with metformin hydrochloride (Metf), its adsorption has studied at different concentrations and pHs, optimal adsorption conditions were determined. Hybrid MSNPs-Metf were mixed with chitosan to compress them and form quasi-spherical pellets, were coated with five chitosan layers as a barrier to prolong metformin release. It showed that this pellet is useful for metformin controlled release since drug over time was significantly delayed by the chitosan coating and then, as metformin is electrostatically linked to MSNPs, it also controls the release of drug, releasing 170 mg after 17 h of exposure at pH 1.2. When pH is > 1.2, metformin release was significantly prolonged. Since 170 mg is 21% of a 850-mg metformin dose and previous studies report that 90% of metformin is recovered as unchanged drug in urine after 12 h of metformin intakes. These results suggest that MSNPs-Metf pellets, coated with chitosan, are an option to avoid excessive metformin ingest.

1. Introduction

Diabetes mellitus is a global health problem due to its elevated prevalence and disability produced. It is one of the main morbidity and mortality cause; nearly 8.3% of the world's population suffers from this disease, its origin lies in some factors such as obesity and sedentary lifestyle (Wild et al., 2004). *Diabetes mellitus* developing serious diseases affecting heart, blood vessels, teeth, kidneys, eyes, nerves and developing infections, which shortens life expectancy (Chacko, 2016), it is caused by a multifarious metabolic disorder characterized by defects in insulin secretion and/or the insulin action, causing hyperglycemia, where fasting plasma glucose concentration is above 1.26 g/L or above 2.00 g/L in blood at any time (Viswanatha et al., 2017).

Metformin hydrochloride (Metf) is one of the most widely used agents for *Diabetes mellitus* control, it is an oral antihyperglycemic that improves glucose tolerance in patients by decreasing basal and postprandial plasma glucose. Metformin acts through three mechanisms: first, reduces hepatic glucose production by inhibiting hypoglycemia and avoids hyperinsulinemia; second, it increases insulin sensitivity in muscle and improves peripheral glucose uptake and utilization; third, it delays the intestinal absorption of glucose. During controlled clinical

trials of metformin (850 mg) three times daily, peak plasma levels are reached between 2.5 and 3.0 h after ingestion and do not exceed 590–1300 ng/mL with half-life between 1.5 and 4.5 h, reaching a lower concentration in blood than in plasma (Moffat et al., 2006). Metformin kinetics are characterized by slow and incomplete absorption (bioavailability 50–60%), from an oral dose of about 30 to 50% is excreted unchanged in urine within 24 h and about 30% in feces (Moffat et al., 2006).

Traditional doses to eliminate pain or infections require high medication levels, generating toxicity, to keep low drug level in serum lower levels than the required dose are provided, causing drug resistance. A local system that delivers medication could correct these inconvenient of traditional dosing (Warren et al., 2008). A problem is presented when drugs are ingested orally, they could dissolve rapidly in the stomach producing blood level peaks and may not produce adequate levels. In addition, when drug blood level is adequate, it begin to decrease and becomes necessary to ingest another dose in a few hours. It is a problem since some drugs are irritating to the stomach or may produce undesirable side effects. The need to release drugs in a gradual or sustained way has given rise to exhaustive research that has generated different solutions, among them arise the possibility of coating the

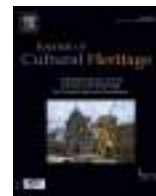
* Corresponding author.

E-mail address: roos_ph@iqcelaya.itc.mx (R. Patiño-Herrera).



Available online at
ScienceDirect
www.sciencedirect.com

Elsevier Masson France
EM|consulte
www.em-consulte.com/en



Original article

Determination of the layered structure of baryta based heritage photographs by infrared ellipsometry



J.M. Flores-Camacho^{a,*}, A. Nieto-Villena^{c,b}, J.R. Martínez^d, J.A. de la Cruz-Mendoza^e,
 G. Ortega-Zarzosa^d, Á. Solbes-García^c, R.E. Balderas-Navarro^a, A. Lastras-Martnez^a

^a Instituto de Investigación en Comunicación Óptica, Universidad Autónoma de San Luis Potosí, Av. Karakorum 1470, 78210 San Luis Potosí, S.L.P., Mexico

^b Departamento de Conservación y Restauración de Bienes Culturales, Universitat Politècnica de València, Camino de Vera s/n, 46022 Valencia, Spain

^c Facultad del Hábitat, Universidad Autónoma de San Luis Potosí, Álvaro Obregón 64, 78000 San Luis Potosí, S.L.P., Mexico

^d Facultad de Ciencias, Universidad Autónoma de San Luis Potosí, Álvaro Obregón 64, 78000 San Luis Potosí, S.L.P., Mexico

^e Instituto de Física, Universidad Autónoma de San Luis Potosí, Álvaro Obregón 64, 78000 San Luis Potosí, S.L.P., Mexico

ARTICLE INFO

Article history:

Received 15 February 2018

Accepted 13 September 2018

Available online 15 October 2018

Keywords:

Photographic Prints

Infrared ellipsometry

Gelatin

Baryta

Julian Carrillo

ABSTRACT

Variable angle-infrared spectroscopic ellipsometry is proposed as a reliable tool for the characterization of heritage photographic prints. It is shown that the proposed technique has access to both the chemical composition and the physical structure of the photograph. In particular, the physical structure can be determined by interference related spectral oscillations and the behavior, for different angles of incidence, of the peaks corresponding to different chemical components. Emphasis is made on gelatin/baryta samples, and particularly, in the role of the baryta layer. A relatively simple model is used to simulate the ellipsometric spectra. It shows that the thickness and location of different layers in photographic prints can be assessed by optical means.

© 2018 Elsevier Masson SAS. All rights reserved.

1. Research aim

The aim of the present work is to present variable-angle infrared-ellipsometry (IRSE) as a reliable tool for the characterization of heritage photographic prints that complements the information obtained from traditional techniques such as Fourier-transform infrared spectroscopy and Raman. IRSE has access to amplitude and phase of light signals, when combined with incidence of probing light at different angles, permits the determination of the chemical composition and the multilayered structure of the print.

2. Introduction

The artistic and documental value of photographic prints, in particular those from the turn of the 20th century, makes it necessary to take actions for their preservation, which requires an in-depth knowledge of the chemical composition and physical structure of these objects [1]. Access to this information has been

successfully provided by analytical techniques such as electron microscopies, atomic force microscopy, Raman spectroscopy, and Fourier-Transform Infrared spectroscopy (FTIR), among others [1]. Of special interest are those of non-invasive and non-destructive character such as the spectroscopic optical techniques. In particular, FTIR has been used for the identification of pigments and organic components in the photographic colloid [2–4], for identification of organic varnishes [5] possibly used as protective coatings, for the detection of the presence of the baryta layer and, combined with other analyses, identification of sources of biological deterioration [6]. The recently explored terahertz spectral region can be used for the characterization of the paper substrate [7].

Gelatin and colloidion aristotypes were the first kind of photographic papers in which the paper support was submitted to a treatment based on the application of a layer of barium sulfate [8]. This technique was later passed on to the more contemporary silver bromide emulsions based *developing out papers*. The baryta paper [9] provided a better finishing of the print [8] and a separation of the emulsion layer from contaminants of the paper support [6]. The barium sulfate pigment was commonly suspended in gelatin; however, it has been known that gum arabic and albumen were also part of this layer. Wax, casein, milk, and starch, among others, were later introduced in the formulation [8]. The baryta layer was composed mostly of BaSO₄, but SrSO₄ and titanium dioxide were also part of

* Corresponding author.

E-mail addresses: jmflores@cactus.iico.uaslp.mx (J.M. Flores-Camacho), alejandra.nieto@uaslp.mx (A. Nieto-Villena).



Effects of Mg incorporation in cubic GaN films grown by PAMBE near Ga rich conditions



V.D. Compeán-García^a, H. Moreno-García^b, E. López-Luna^b, H. Pérez Ladrón de Guevara^c,
A. Escobosa Echavarría^d, Y. Kudriavtsev^d, F.J. Rodríguez-Aranda^b, A.G. Rodríguez^b, M.A. Vidal^{b,*}

^a CONACyT-Coordinación para la Innovación y Aplicación de la Ciencia y Tecnología (CIACyT), Universidad Autónoma de San Luis Potosí (UASLP), Álvaro Obregón 64, San Luis Potosí 78000, Mexico

^b Coordinación para la Innovación y Aplicación de la Ciencia y Tecnología (CIACyT), Universidad Autónoma de San Luis Potosí (UASLP), Álvaro Obregón 64, San Luis Potosí 78000, Mexico

^c Centro Universitario de los Lagos, Universidad de Guadalajara, Av. Enrique Díaz de León 1144, col. Paseos de la Montaña, Lagos de Moreno, Jalisco 47460, Mexico

^d Electric Engineering Department, Centro de Investigación y Estudios Avanzados del IPN, Apartado Postal 14-740, 07000 México D.F., Mexico

ARTICLE INFO

Keywords:

Cubic GaN diode
Mg p-type doping
Plasma-assisted molecular beam epitaxy

ABSTRACT

The structural and electrical properties of Mg-doped cubic GaN epi-layers grown by plasma-assisted molecular beam epitaxy (PAMBE) near Ga rich conditions are investigated. The diffraction of high-energy reflected electrons (RHEED) in situ, in addition to structural studies of X-ray diffraction, show that the fraction of hexagonal and crystal twinning inclusions decreases when the Mg flux increases. The condition for the higher incorporation of Mg where the electrical properties are optimized is highly sensitive to the flow ratio Mg/Ga. The p-doping level steadily increases with increasing Mg flux. The Mg concentration obtained by secondary ion mass spectroscopy (SIMS) from samples grown at Mg temperatures from 200 °C to 700 °C are in a range between 2×10^{19} to 2×10^{20} atoms/cm³. The highest mobility and p-type doping level achieved, determined from Hall measurements, were 28.2 cm²/V-s and 2×10^{19} cm⁻³, respectively. We corroborate that the Mg doped c-GaN films are suitable for the construction of optoelectronic devices based on cubic III-Nitrides.

1. Introduction

Cubic gallium nitride (c-GaN) has a bandgap of 200 meV lower than the hexagonal phase (h-GaN) [1], for this reason, it is possible to modulate to the visible region with less amount of indium in the zinc-blend than wurtzite InGaN alloy [2–5]. In addition, due to higher crystalline symmetry, resulting in more isotropic properties and no spontaneous polarization induced-electric fields in the direction parallel to the c-axis, it is possible to grow the cubic InGaN alloy with a bandgap in the green region [2–9]. Consequently, this alloy is attractive for applications in photovoltaic and optoelectronic devices, including multiband solar cells, hydrogen production photoelectrodes, laser and light emitting diodes [10].

However, the development of optoelectronic, photovoltaic and electronic devices based on c-InGaN requires an efficient p-type doping and high-quality crystal structure. To our knowledge, limited reports of cubic III-Nitrides devices have been found in the literature [11,12], this is in part for the inefficient p-type doping or the main disadvantage in the synthesis of c-GaN, the lack of native substrates and a low-quality

crystalline film due to the hexagonal inclusions [13,14]. Therefore, improvements in the efficiency of p-type doping of the c-GaN epilayers are essential for enhanced manufacturing technology of cubic III-Nitrides semiconductors.

This paper presents a study of the influence of the Mg flux on the electrical and structural properties of Mg doping c-GaN, grown by molecular beam epitaxy on MgO (100) substrates, near to the regimen of Ga rich conditions. This study is performed by varying the Mg flux (with magnesium effusion cell temperature in a range from 200 to 700 °C) with growth conditions of c-GaN films at 720 °C.

2. Experimental

Epitaxial growth of Mg-doped c-GaN films heterostructures under study was performed on 1 cm² MgO(001) substrates by a vertical PAMBE with standard effusion cells for Ga, Mg, and an high-purity N₂ RF plasma cell [2,6]. The purity of Ga and Mg sources are 99.9995%.

Prior to the growth of the Mg-doped GaN epi-layer, the substrate was cleaned on a 10 min trichloroethylene and acetone ultrasonic bath.

* Corresponding author.

E-mail address: miguel.vidal@uaslp.mx (M.A. Vidal).

<https://doi.org/10.1016/j.mssp.2018.12.019>

Received 8 November 2018; Received in revised form 17 December 2018; Accepted 19 December 2018

Available online 11 January 2019

1369-8001/ © 2018 Published by Elsevier Ltd.



Promotional effect of metal doping on nanostructured TiO₂ during the photocatalytic degradation of 4-chlorophenol and naproxen sodium as pollutants



Mariana Hinojosa – Reyes^{a,b,*}, Roberto Camposeco – Solis^c, Facundo Ruiz^b,
Vicente Rodríguez – González^d, Edgar Moctezuma^a

^a Facultad de Ciencias Químicas, Universidad Autónoma de San Luis Potosí, Av. Manuel Nava # 6, San Luis Potosí, S.L.P., 78290, Mexico

^b Facultad de Ciencias, Universidad Autónoma de San Luis Potosí, San Luis Potosí, SLP, 78000, Mexico

^c Instituto de Ciencias Aplicadas y Tecnología, Universidad Nacional Autónoma de México, Circuito Exterior S/N, Ciudad Universitaria, A. P. 70-186, Delegación Coyoacán, C.P. 04510, México D. F., Mexico

^d División de Materiales Avanzados, IPICYT, Instituto Potosino de Investigación Científica y Tecnológica, Camino a la Presa San José 2055, Col. Lomas 4a. Sección, C.P. 78216, San Luis Potosí, S.L.P., Mexico

ARTICLE INFO

Keywords:

Doped titania
4-Chlorophenol
Naproxen sodium
Kinetics
Photocatalysis
Reusability test

ABSTRACT

Titania doped nanomaterials were prepared by the sol – gel method. Nickel, copper and iron were employed as doping cations. The as-prepared materials were characterized by X-ray diffraction, N₂ physisorption and UV–vis DRS, EDS and XPS techniques. The TiO₂-doped materials were evaluated during the photocatalytic degradation of 4-chlorophenol (4-CP) and naproxen (NPX) sodium as water pollutants under UV radiation. According to the photocatalytic activity and kinetic results, T-Cu 1.0 was the material with the best performance during the degradation of 4-CP, showing a degradation performance of 90% (0.1827 L g⁻¹ min⁻¹) after six reaction hours. T-Fe 1.0 was the photocatalyst with the best NPX degradation behavior, showing a degradation efficiency of 97% (0.1111 L g⁻¹ min⁻¹) also after 6 reaction hours. The photocatalytic degradations followed a *pseudo*-first-order behavior. The remarkable performance of the photocatalysts was due to a higher concentration of Ti³⁺ species and the presence of Ni²⁺, Cu²⁺ and Fe³⁺, which worked as TiO₂ heterojunctions that allowed the degradation improvement of the organic compounds. The T-Cu 1.0 and T-Fe 1.0 materials were used in a reusability test for 4-CP and NPX compounds, showing around 20 and 30% of final deactivation, respectively. This deactivation was due to structural changes in the TiO₂ framework and the oxidation state of the doping cation as a consequence of the constant exposure to UV radiation (18 h) and to the accumulation of carbonaceous species on the TiO₂ surface. The systematic XPS analysis before and after the photocatalytic evaluation reveals its internal structure and gives insights about its photocatalytic behavior.

1. Introduction

Titania nanomaterials have been employed widely during the photocatalytic degradation of numerous organic compounds. The advantages of using TiO₂ are its low cost, non-toxicity, high stability and above all, it has excellent physicochemical properties [1].

TiO₂ is a semiconductor with valence and conduction bands with values of -7.6 and -4.4 eV, respectively, giving a resultant band gap value of 3.2 eV [2]. This band position has enough energy to produce reactive oxygen species (ROS) which include highly reactive oxygen atoms, free radicals, singlet molecular dioxygen, hydrogen peroxide, as well as other peroxides, both inorganic and organic hydroxyl and

superoxide radicals (HO•, O²⁻, HOO•, H₂O₂) [3]. Numerous reports have been published about its use in the photocatalytic degradation of a wide variety of contaminants (dyes, drugs, personal products, pesticides, antibiotics and endocrine disruptors, among others).

Nevertheless, TiO₂ has the disadvantage of hole-electron recombination, causing a decrease in the photocatalytic activity. To overcome this effect, the TiO₂ nanomaterials have been modified or impregnated superficially with metallic nanoparticles or other semiconductor oxides. In order to improve the photoefficiency of the electronic process, TiO₂ has been doped with transition metals or defects have been introduced into its structure, which has been widely employed due to the formation of heterojunctions. The origin of these

* Corresponding author. Facultad de Ciencias Químicas, Universidad Autónoma de San Luis Potosí, Av. Manuel Nava # 6, San Luis Potosí, S.L.P., 78290, Mexico.
E-mail addresses: kittyhinojosa@hotmail.com, mariana.hinojosa.reyes@gmail.com (M. Hinojosa – Reyes).

<https://doi.org/10.1016/j.mssp.2019.04.050>

Received 19 December 2018; Received in revised form 3 April 2019; Accepted 30 April 2019

Available online 10 May 2019

1369-8001/ © 2019 Elsevier Ltd. All rights reserved.



Surface-enhanced raman spectroscopy: A non invasive alternative procedure for early detection in childhood asthma biomarkers in saliva



B.N. Zamora-Mendoza^a, R. Espinosa-Tanguma^b, M.G. Ramírez-Elías^c, R. Cabrera-Alonso^d, G. Montero-Moran^a, D. Portales-Pérez^a, J.A. Rosales-Romo^e, J.F. Gonzalez^d, C. Gonzalez^{a,*}

^a Universidad Autonoma de San Luis Potosí, Facultad de Ciencias Químicas, Av. Dr. Manuel Nava #6, San Luis Potosí, 78210, Mexico

^b Universidad Autonoma de San Luis Potosí, Facultad de Medicina, Av. Venustiano Carranza #2405, San Luis Potosí, 78210, Mexico

^c Universidad Autonoma de San Luis Potosí, Facultad de Ciencias, Av. Chapultepec #1570Privadas del Pedregal, San Luis Potosí, 78290, Mexico

^d Universidad Autonoma de San Luis Potosí, Coordinación para la Innovación y Aplicación de la Ciencia y la Tecnología (CIACyT), Av. Sierra Leona #550, San Luis Potosí, 78210, Mexico

^e Servicios de Salud de San Luis Potosí, Hospital General de Soledad de Graciano Sánchez, Prolongación Valentín Amador #1112, Colonia Genovevo Rivas Guillen, Soledad de Graciano Sánchez, San Luis Potosí, 78432, Mexico

ARTICLE INFO

Keywords:

Asthma
saliva
SERS
Cytokines
Raman Spectroscopy

ABSTRACT

The early detection of bronchial inflammation in asthma, through a non-invasive, simple method and under a subclinical state, could lead to a more effective control of this condition. The aim of this study was to identify biomarkers of bronchial inflammation in the saliva of children with asthma through immunoassay and Surface Enhanced Raman Spectroscopy (SERS). We conducted an analytical cross-sectional study in 44 children ages 6–12; the diagnosis of asthma was made according to Global Initiative for Asthma (GINA) standards. The children's saliva was analyzed by immunoassay for the quantification of 37 cytokines, as well as SERS analysis in a confocal Raman microscope at 785 nm. We found a significant association between bronchial obstruction and IL-8 ($p = 0.004$), IL-10 ($p = 0.008$) and sCD163 ($p = 0.003$). The Raman spectra showed significant amplification in the region of 760 to 1750 cm^{-1} . The Principal Component Analysis and Linear Discriminant Analysis (PCA-LDA) method has a sensitivity of 85%, specificity of 82% and an accuracy of 84% for the diagnosis of asthma. These results demonstrate the presence of a subclinical inflammatory state, suggestive of bronchial remodeling in the population studied. The SERS method is a potential tool for identifying bronchial inflammation and its endotype, allowing for a highly sensitive and specific diagnosis.

1. Introduction

Asthma is evidenced by the result of forced spirometry, with post-bronchodilator reversibility $> 12\%$ forced expiratory volume in the first second (FEV_{1}). This condition, which affects more than 300 million people worldwide, is the leading cause of childhood morbidity in Latin America with a prevalence of 5.7–16% among 4–8 years [1,2]. This emphasizes the importance of making an opportune diagnosis to apply specific pharmacological therapy, as well as effective monitoring and control of this disease. The aim of the present work was to identify cytokines as potential biomarkers using a non-invasive method through SERS, in relation to cytokine profiles obtained by immunoassay for the early detection of bronchial inflammation.

The interactions between predisposing factors and signaling pathways of bronchial cells, especially in the immune system, explain the

heterogeneous clinical expression, known as phenotype, which can occur in each patient. One or more endotypes are present within the phenotype when the inflammatory response is mediated by several cellular signaling pathways [2,3]. Likewise, this heterogeneity has allowed the identification of over 100 biomarkers for this condition, among which proinflammatory cytokines secreted by helper 1 and 2 T lymphocytes (Th1/Th2) play an important role in bronchial inflammation. These are proteins which participate in the differentiation and maturation of immune system cells [4,5] contributing to communication between them, and in some cases acting directly on those patients with severe asthma, difficult to control asthma and poor response to treatment. These cytokines are able to travel through the bloodstream and cross permeable biological barriers [6,7], thus making it possible to detect them in saliva and other biological fluids.

It has been shown that in patients with asthma the number of

* Corresponding author.

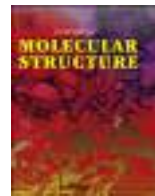
E-mail address: gonzalez.castillocarmen@uaslp.mx (C. Gonzalez).

<https://doi.org/10.1016/j.pdpdt.2019.05.009>

Received 12 December 2018; Received in revised form 28 March 2019; Accepted 9 May 2019

Available online 10 May 2019

1572-1000/ © 2019 Elsevier B.V. All rights reserved.



Characterizing the properties of anticancer silibinin and silybin B complexes with UV–Vis, FT-IR, and Raman spectroscopies: A combined experimental and theoretical study



A. Solís-Gómez^{a, **}, R.Y. Sato-Berrú^a, M.E. Mata-Zamora^a, J.M. Saniger^a,
R.A. Guirado-López^{b, *}

^a Instituto de Ciencias Aplicadas y Tecnología, Universidad Nacional Autónoma de México, Circuito Exterior s/n, Ciudad Universitaria, Delegación Coyoacán, C.P. 04510 Ciudad de México, Mexico

^b Instituto de Física “Manuel Sandoval Vallarta”, Universidad Autónoma de San Luis Potosí, Álvaro Obregón 64, San Luis Potosí, S.L.P., 78000, Mexico

ARTICLE INFO

Article history:

Received 31 October 2018

Received in revised form

7 January 2019

Accepted 11 January 2019

Available online 12 January 2019

Keywords:

Silybin

UV–Vis

Infrared spectroscopy

Raman spectroscopy

Density functional theory

Circular dichroism

ABSTRACT

We present a combined experimental and theoretical study dedicated to analyze the structure, optical properties, and vibrational behavior of the anticancer silibinin complex and one of its molecular constituents, namely; silybin B. A comparison of the UV–Vis and FT-IR characterization of these samples reveals the presence of almost identical features. In both cases, the existence of four absorption maxima located at 204, 230, 287, and 330 nm are observed, as well as vibrational bands that show a complex distribution in the 300–1700 cm^{-1} frequency domain together with three infrared excitations placed at ~3180, 3450, and 3600 cm^{-1} typically associated with different C–H and O–H bond vibrations. For the first time, we present the Raman spectra of these samples. Interestingly, the Raman response reveals more notable differences between the two molecular complexes, mainly in the 300–900 cm^{-1} frequency range. Furthermore, we obtain that the wavelength of the excitation laser plays a fundamental role in revealing precise features of the spectra. Based on density functional theory (DFT) calculations we also simulate the UV–Vis, circular dichroism, infrared, and Raman spectra of model silybin A and silybin B ($\text{C}_{25}\text{H}_{22}\text{O}_{10}$) molecules in both isolated and aggregated forms. An excellent agreement is found when contrasting experimental and theoretical data. Based on this comparison, we identify the main infrared- and Raman-active vibrational modes of silybin B, and infer those frequencies that seems to be unique to silybin A. Wavelength dependent calculations of the Raman spectra also reveal the crucial role played by the energy of the incident laser in determining the intensities of the Raman active modes, allowing for a better comparison between theory and experiment. Finally, simulations of the circular dichroism spectra for isolated silybin A and B species reveal clear differences between the two molecules, being thus an appropriate tool to distinguish the presence of specific isomers in a sample.

© 2019 Elsevier B.V. All rights reserved.

1. Introduction

Plant-derived compounds can provide us with unlimited opportunities for new drug discoveries due to their wide range of biological and chemical activities [1]. Plants contain a large variety of substances having different density distribution, structure, and tissue localization. Following their chemical structure, they can be

organized into various categories such as chromones, carotenoids, flavonoids, alkaloids, etc. Among the previous constituents, flavonoids have been the subject of intense investigations in the last years due to their possible use as free radical scavengers [2–4], antioxidants [5,6], antimicrobial complexes [7], and as secondary agents in chemo combination strategies to treat prostate, breast, as well as lung cancer [8]. The previous biological activity has been assumed to be strongly correlated to the presence of carbonyl and hydroxyl groups in the carbon skeleton characterizing flavonoids, and to the way these groups interact with the surrounding media. It is important to precise that flavonoids are poorly water soluble, a property that seriously limits the applications mentioned above

* Corresponding author.

** Corresponding author.

E-mail addresses: solis.ga@gmail.com (A. Solís-Gómez), guirado@ifisica.uaslp.mx (R.A. Guirado-López).

Partial Image Encryption Using Cellular Automata

Marco Tulio Ramírez Torres¹, Marcela Mejía Carlos², José S. Murguía Ibarra³, Luis Javier Ontañón García¹

¹ Universidad Autónoma de San Luis Potosí, CARAO,
México

² Universidad Autónoma de San Luis Potosí, IICO,
México

³ Universidad Autónoma de San Luis Potosí,
Facultad de Ciencias,
México

{tulio.torres, marcela.mejia, ondeleto, luis.ontanon}@uaslp.mx

Abstract. In this work is proposed a partial image encryption method based on the synchronization of the cellular automaton rule 90. The security analysis proves that this cryptosystem is resistant to different tests and attacks such as the Chosen/Knownplain image attack and bit-replacement. This algorithm is a variant from another encryption algorithm named ESCA, in this case we modified the ESCA system to a partial encryption version reducing the latency time up to a 50%. This version has two changes a) it only encrypts the three most significant bits, and b) the bits of the secret key are rotated instead of calculating a key for each block of plaintext. These changes allow to reduce the latency time and according to the tests do not compromise the security. This proposal could be a feasible and secure option for real-time applications.

Keywords. Partial encryption, digital images, cellular automata.

1 Introduction

Nowadays, many of our information is in digital formats and it is sent through networks or is stored in different devices. And, with technologies as Internet of things our personal data could be more and more exposed, therefore we need to learn about internet and its risks [14] and develop new security techniques. For this reason, it exists a great interest in the protection and manipulation of the data.

Due to the great advances in technology, each time is required to have better and more efficient algorithms for confidential and secure data handling. This information may vary depending on the application area and in many cases is necessary processing it in real time.

For example, pictures, medical images, diagrams, surveillance video, video conference, etc. could contain confidential information, and if these data are transmitted and are not encrypted the confidentiality of information is exposed in the links allowing access to third parties without being detected. To overcome the eavesdropping problem several encryption systems have been proposed, such as AES (Advanced Encryption Standard), IDEA (International Data Encryption Algorithm), RSA (Rivest, Shamir y Adleman) among others.

These systems are generally used in text and binary data, but they are not suitable for the encryption of multimedia content as digital images and audio files, due to their massive volumes, high adjacent correlation and sometimes the multimedia data require real-time interactions (displaying, bit rate conversion, etc.) [3]. That is why the image encryption is a particular studying area. The image encryption algorithms should provide two kinds of security: cryptographic security and perceptual security.

CLOSING IN ON HILL'S CONJECTURE*

JÓZSEF BALOGH[†], BERNARD LIDICKÝ[‡], AND GELASIO SALAZAR[§]

Abstract. Borrowing László Székely's lively expression, we show that Hill's conjecture is “asymptotically at least 98.5% true.” This long-standing conjecture states that the crossing number $\text{cr}(K_n)$ of the complete graph K_n is $H(n) := \frac{1}{4} \lfloor \frac{n}{2} \rfloor \lfloor \frac{n-1}{2} \rfloor \lfloor \frac{n-2}{2} \rfloor \lfloor \frac{n-3}{2} \rfloor$ for all $n \geq 3$. This has been verified only for $n \leq 12$. Using the flag algebra framework, Norin and Zwols obtained the best known asymptotic lower bound for the crossing number of complete bipartite graphs, from which it follows that for every sufficiently large n , $\text{cr}(K_n) > 0.905 H(n)$. Also using this framework, we prove that asymptotically $\text{cr}(K_n)$ is at least $0.985 H(n)$. We also show that the spherical geodesic crossing number of K_n is asymptotically at least $0.996 H(n)$.

Key words. crossing number, complete graph, Hill's conjecture, flag algebras

AMS subject classifications. 05C10, 05C62, 68R10

DOI. 10.1137/17M1158859

1. Introduction. A long-standing open problem in topological graph theory is to determine the crossing number of the complete graph K_n . We recall that the *crossing number* $\text{cr}(G)$ of a graph G is the minimum number of pairwise crossings of edges in a drawing of G in the plane.

1.1. Our main results. As narrated in the illustrative survey by Beineke and Wilson [14], the problem of estimating the crossing number of complete graphs seems to have been first explored by the British artist Anthony Hill in the late 1950s. Hill found a construction that yields a drawing of K_n with exactly $\frac{1}{4} \lfloor \frac{n}{2} \rfloor \lfloor \frac{n-1}{2} \rfloor \lfloor \frac{n-2}{2} \rfloor \lfloor \frac{n-3}{2} \rfloor$ crossings for every integer $n \geq 3$ [24]. In that paper, the following conjecture was put forward.

Conjecture (Hill's conjecture).

$$\text{cr}(K_n) = H(n) := \frac{1}{4} \left\lfloor \frac{n}{2} \right\rfloor \left\lfloor \frac{n-1}{2} \right\rfloor \left\lfloor \frac{n-2}{2} \right\rfloor \left\lfloor \frac{n-3}{2} \right\rfloor.$$

As we recall below in our discussion of previous work, Hill's conjecture has only been verified for $n \leq 12$, and it follows from the work by Norin and Zwols [34] that $\lim_{n \rightarrow \infty} \text{cr}(K_n)/H(n) > 0.905$. Our main result in this paper is the following.

THEOREM 1.

$$\lim_{n \rightarrow \infty} \frac{\text{cr}(K_n)}{H(n)} > 0.98559895.$$

We also investigate spherical drawings of K_n . We recall that in a *spherical geodesic* drawing of a graph, the host surface is the sphere, and each edge is a minimum distance

*Received by the editors November 27, 2017; accepted for publication (in revised form) April 23, 2019; published electronically July 18, 2019.

<https://doi.org/10.1137/17M1158859>

Funding: The first author's research was partially supported by NSF grant DMS-1500121 and the Langan Scholar Fund (UIUC). The second author's research was supported in part by NSF grant DMS-1600390. The third author's research was supported by CONACYT grant 222667.

[†]Department of Mathematical Sciences, University of Illinois at Urbana-Champaign, Urbana, IL 61801 (jobal@math.uiuc.edu).

[‡]Department of Mathematics, Iowa State University, Ames, IA 50011 (lidicky@iastate.edu).

[§]Instituto de Física, Universidad Autónoma de San Luis Potosí, San Luis Potosí, Mexico (gsalazar@ifisica.uaslp.mx).



When can a link be obtained from another using crossing exchanges and smoothings?



Carolina Medina ^a, Gelasio Salazar ^{b,*}

^a Department of Mathematics, University of California, Davis, Davis, CA 95616, USA

^b Instituto de Física, Universidad Autónoma de San Luis Potosí, San Luis Potosí, Mexico

ARTICLE INFO

Article history:

Received 11 March 2019

Received in revised form 25 March 2019

Accepted 26 March 2019

Available online 29 March 2019

MSC:

57M25

Keywords:

Knot diagrams

Knot projections

Partial order

Smoothing order

Plane graphs

Graph minors

ABSTRACT

Let L be a fixed link. Given a link diagram D , is there a sequence of crossing exchanges and smoothings on D that yields a diagram of L ? We approach this problem from the computational complexity point of view. It follows from work by Endo, Itoh, and Taniyama that if L is a prime link with crossing number at most 5, then there is an algorithm that answers this question in polynomial time. We show that the same holds for all torus links $T_{2,m}$ and all twist knots.

© 2019 Published by Elsevier B.V.

1. Introduction

We work in the piecewise linear category. All links under consideration are nonsplit, unordered, unoriented and contained in the 3-sphere S^3 . We remark that when we speak of a link L we include the possibility that L is a link with only one component, that is, a knot. All diagrams under consideration are regular diagrams in the 2-sphere $S^2 \subset S^3$.

This work revolves around the following basic question. Let L be a fixed link. Given a link diagram D , does there exist a sequence of crossing exchanges and smoothings on D that yields a diagram of L ? If this is the case, then for brevity we write $D \rightsquigarrow L$ (Fig. 1).

One wonders how “difficult” this question is. To formalize this, we need to work under the computational complexity setting, posing this question in the standard form of a decision problem.

* Corresponding author.

E-mail addresses: cmolina@math.ucdavis.edu (C. Medina), gsalazar@ifisica.uaslp.mx (G. Salazar).



Embeddability of Arrangements of Pseudocircles and Graphs on Surfaces

Éric Colin de Verdière¹ · Carolina Medina² · Edgardo Roldán-Pensado³ · Gelasio Salazar⁴

Received: 1 January 2019 / Revised: 20 July 2019 / Accepted: 11 August 2019
© Springer Science+Business Media, LLC, part of Springer Nature 2019

Abstract

A pseudocircle is a simple closed curve on some surface; an arrangement of pseudocircles is a collection of pseudocircles that pairwise intersect in exactly two points, at which they cross. Ortner proved that an arrangement of pseudocircles is embeddable into the sphere if and only if all of its subarrangements of size at most four are embeddable into the sphere, and asked if an analogous result holds for embeddability into orientable surfaces of higher genus. We answer this question positively: An arrangement of pseudocircles is embeddable into an orientable surface of genus g if and only if all of its subarrangements of size at most $4g + 4$ are. Moreover, this bound is tight. We actually have similar results for a much general notion of arrangement, which we call an *arrangement of graphs*.

Keywords Arrangements of pseudocircles · Graph embeddings · Graphs on surfaces · Arrangements of graphs

Dedicated to the memory of Branko Grünbaum.

Editor in Charge: Kenneth Clarkson

Éric Colin de Verdière
eric.colindeverdiere@u-pem.fr

Carolina Medina
cmedina@math.ucdavis.edu

Edgardo Roldán-Pensado
e.rolدان@im.unam.mx

Gelasio Salazar
gsalazar@ifisica.uaslp.mx

¹ Université Paris-Est, LIGM, CNRS, ENPC, ESIEE Paris, UPEM, Marne-la-Vallée, France

² Instituto de Física, UASLP, 78000 San Luis Potosí, Mexico

³ Centro de Ciencias Matemáticas, UNAM Campus Morelia, 58190 Morelia, Michoacán, Mexico

⁴ Instituto de Física, UASLP, 78000 San Luis Potosí, Mexico



Research paper

The role of solvent quality, inhomogeneous polymer brush composition, grafting density and number of free chains on the viscosity, friction between surfaces, and their scaling laws



R. Catarino Centeno^{a,b,c}, M.A. Balderas Altamirano^c, E. Pérez^d, A. Gama Goicochea^{c,e,*}

^a División de Ingeniería Mecatrónica, Instituto Tecnológico Superior de Zacapoaxtla, Zacapoaxtla 73680, Puebla, Mexico

^b Posgrado en Ciencias Aplicadas, Facultad de Ciencias, Universidad Autónoma de San Luis Potosí, San Luis Potosí 78290, San Luis Potosí, Mexico

^c Posgrado en Ingeniería Química, División de Ingeniería Química y Bioquímica, Tecnológico de Estudios Superiores de Ecatepec, Ecatepec 55210, Estado de México, Mexico

^d Instituto de Física, Universidad Autónoma de San Luis Potosí, San Luis Potosí 78000, San Luis Potosí, Mexico

^e Reservoir Engineering Research Institute, Palo Alto, CA 94301, USA

HIGHLIGHTS

- Mixed polymer brushes can reduce friction between surfaces more than pure ones.
- A critical grafting density is found for each type of composition.
- Viscosity and friction obey scaling laws that depend on solvent quality only.
- An optimal mixed brush composition is predicted, for polymers used in industry.

ARTICLE INFO

Keywords:

Inhomogeneous polymer brushes

Couette flow

Dissipative particle dynamics

Friction coefficient

Viscosity

Scaling

ABSTRACT

Brushes made up of mixtures of polymers are modeled using mesoscale simulations under shear and the viscosity and the friction coefficient are obtained as functions of the chains' grafting density, brush composition, free chain concentration, and solvent quality. We find that brushes made up of mixtures of polymers can reduce to a greater extent the friction coefficient in comparison to a mono-chain brush and that both the viscosity and the friction coefficient obey scaling laws that depend *only* on solvent quality. These results shed light on microscopic mechanisms that affect viscosity and friction in polymeric brushes, which are findings of interest for research on nanotribology.

1. Introduction

In recent years attention has focused on the design of functionalized surfaces by grafting polymers on surfaces using effective numerical tools [1,2], which has attracted attention in applications such as stabilizing colloids [3], improving lubrication properties when surfaces are exposed to shear, and protecting the surface against adsorption of nanoparticles due to the response to non-equilibrium dynamics [4,5]. It is well known that surfaces coated with polymeric brushes in a good solvent have excellent tribological properties, when subject to flow [6–13]. Goujon and coworkers [14–16] have described the rheology of the system by studying the influence of free chains on the friction and viscosity, finding that the friction coefficient (COF) decreases linearly

with the surface coverage when no detachment is considered and when few chains are expelled from the brush, the friction decreases significantly reaching an asymptotic value.

The interaction of a polymer brush in the presence of free chains is of great interest because of the change in the wetting properties of the surface and has been widely studied using various theoretical and simulation methods [17–19]. Additionally, the mechanical and rheological properties of the brushes are of importance, because the presence of grafted chains can reduce the friction between two surfaces by three orders of magnitude [4,15]. In works by Singh et al. [6,20], the effect of grafting density and chain stiffness on the tribological behavior of polymer brushes were explored, finding that the COF depends on chain stiffness. Deng et al. [21] modeled functionalized surfaces using

* Corresponding author at: Posgrado en Ingeniería Química, División de Ingeniería Química y Bioquímica, Tecnológico de Estudios Superiores de Ecatepec, Ecatepec 55210, Estado de México, Mexico.

E-mail address: agama@alumni.stanford.edu (A. Gama Goicochea).

<https://doi.org/10.1016/j.cplett.2019.03.002>

Received 31 October 2018; Received in revised form 1 March 2019; Accepted 4 March 2019

Available online 08 March 2019

0009-2614/ © 2019 Elsevier B.V. All rights reserved.



Improvement of the conversion efficiency of as-deposited Bi₂S₃/PbS solar cells using a CeO₂ buffer layer



L.E. Ríos-Saldaña^a, V.D. Compeán-García^b, H. Moreno-García^a, A.G. Rodríguez^{a,*}

^a *Coordinación para la Innovación y la Aplicación de la Ciencia y la Tecnología (CIACYT), Universidad Autónoma de San Luis Potosí (UASLP), Álvaro Obregón 64, 78000 San Luis Potosí, S.L.P., Mexico*

^b *CONACYT—Coordinación para la Innovación y la Aplicación de la Ciencia y la Tecnología (CIACYT), Universidad Autónoma de San Luis Potosí, Álvaro Obregón 64, 78000 San Luis Potosí, S.L.P., Mexico*

ARTICLE INFO

Keywords:

CeO₂
Solar cell
Chalcogenides

ABSTRACT

We evaluated the performance of CeO₂ as a buffer layer for emerging thin-film solar cells. Thin films of CeO₂ were deposited via spin coating on transparent conductive oxide (TCO) glass substrates. The photovoltaic parameters of open-circuit voltage (V_{oc}), short-circuit current density (J_{sc}), fill factor (FF), and conversion efficiency of the reference samples increased from 134 mV, 4.14 mA/cm², 0.26, and 0.14% to 254 mV, 14.74 mA/cm², 0.34, and 1.27%, respectively, by using the structure TCO/CeO₂/Bi₂S₃/PbS. The crystallite size of the absorber layer (PbS) increased from 14 to 24 nm using a 130 nm CeO₂ buffer layer.

1. Introduction

The global demand for electrical energy increases every year. Finite resources, such as fossil fuels, continue to be the primary sources of power for electricity generation [1]. Therefore, a variety of technologies are being developed to generate electricity from clean energy sources. Among these renewable energy technologies, solar energy is a more reliable method for the clean conversion of energy into electricity. This conversion can be indirectly achieved through solar-thermal technologies or directly through photovoltaic systems. Current commercial photovoltaic devices are mainly based on silicon (Si), cadmium telluride (CdTe), or copper, indium, gallium, and selenium or sulfur (CIGS). While reliable devices can be obtained using these materials, they have certain limitations, such as the complexity of their production or the limited abundance of the component elements in the earth's crust. Thus, further research on the diversification of the materials used for the manufacture of photovoltaic devices is needed to support the large global demand for electrical energy [2]. Based on these challenges, the development of emerging materials for solar energy applications has become widely diversified over the last few decades. For example, Ce-doped ZnO using co-catalyst Cu²⁺ grafting (Cu²⁺-Ce_xZn_{1-x}O) has been considered for photocatalytic applications. The impurity states formed in this material through metal-ion doping has shown a high sensitivity for visible-light absorption [3]. In addition, the further development of other emerging materials has been broadened to include materials using a variety of configurations, such as organic solar

cells, quantum dot solar cells (QDSCs), and colloidal quantum dot solar cells (CQDSCs). A novel organic molecular bis-triphenylamine with a spiro (fluorene-9,9'-xanthene) named BTPA-4 was applied in the ZnO-NWs/PbS-QDs/BTPA-4/Au configuration and reported power conversion efficiency (PCE) values of 5.44% [4]. Some additional novel examples are CdS sensitized TiO₂ nanorod arrays that have been successfully applied on solar cells and CdSe_xS_{1-x}/CdS co-sensitized TiO₂ nanostructures that have been used for energy conversion [5,6]. Recently, several compounds composed of rare earth elements have attracted considerable interest for solar energy applications. In particular, due to its excellent physical and chemical properties, cerium oxide (CeO₂) is valued as a versatile compound that can be used in a variety of applications. CeO₂ is an oxide semiconductor with a wide optical band gap (p-d) of 5.5 eV and an electronic band gap (p-f) of 3.5 eV [6]. For the elaboration of CeO₂ thin films, several synthesis routes have been reported, such as Metal Organic Chemical Vapor Deposition (MOCVD), magnetron sputtering, electron beam evaporation, sol-gel methods, and chemical solution deposition [7–11]. However, chemical routes are considered the most popular because they can easily allow thicknesses in the range from 6 to 100 nm with crystallite sizes from 6 to 21 nm, depending on the technique and deposit conditions [6–11]. Bulk CeO₂ has a cubic crystalline structure (Fm3m space group) with a lattice constant of 0.451 nm [11–15]. There have been few reports on the use of CeO₂ thin films in solar cells, and it has only recently been employed as a buffer or intermediate absorber layer in solar cells. CeO₂/CdS has been included as a 1–5 nm buffer to develop copper, zinc, tin, sulfide

* Corresponding author.

E-mail address: angel.rodriguez@uaslp.mx (A.G. Rodríguez).

<https://doi.org/10.1016/j.tsf.2018.12.017>

Received 23 March 2018; Received in revised form 2 December 2018; Accepted 11 December 2018

Available online 12 December 2018

0040-6090/© 2018 Elsevier B.V. All rights reserved.



Research articles

Magnetic properties of GaAs:Mn self-assembled nanostructures grown at relatively high-temperature by Molecular Beam Epitaxy



A. del Rio-de Santiago^{a,b,*}, C.F. Sánchez-Valdés^c, J.L. Sánchez Llamazares^d, M.A. Vidal^b, V.H. Méndez-García^b, M. López-López^e, E. Cruz-Hernández^{b,*}

^a Unidad Académica de Ingeniería, Universidad Autónoma de Zacatecas, Ramón López Velarde 801, C.P. 98000 Zacatecas, Zac., Mexico

^b Coordinación para la Innovación y Aplicación de la Ciencia y Tecnología (CIACyT), Universidad Autónoma de San Luis Potosí (UASLP), Av. Sierra Leona #550, Lomas 2a Sección, San Luis Potosí, S. L. P. 78210, Mexico

^c División Multidisciplinaria, Ciudad Universitaria, Universidad Autónoma de Ciudad Juárez (UACJ), Calle José de Jesús Macías Delgado # 18100, Ciudad Juárez 32579, Chihuahua, Mexico

^d Instituto Potosino de Investigación Científica y Tecnológica A.C., Camino a la Presa San José 2055, Col. Lomas 4^a sección, San Luis Potosí, S.L.P. 78216, Mexico

^e Physics Department, Centro de Investigación y de Estudios Avanzados del IPN, Apartado Postal 14-740, México D.F. 07000, Mexico

ARTICLE INFO

Keywords:

Magnetic cluster

Self-assembly

Diluted magnetic semiconductor

Nanostructures

ABSTRACT

We report the influence of the Mn atomic concentration (at.%) on the nanostructures formation and magnetic properties of GaAs:Mn layers grown by Molecular Beam Epitaxy at a relatively high substrate temperature of 530 °C varying the nominal Mn at.% content from 0.01 to 0.2. It is shown that by modifying the Mn at.% different kind of nanostructures, ranging from 2D (such as islands and surface corrugation) to 3D microleaves and nanowire-like arrays, form on the surface layer. Samples produced with Mn contents ranging from 0.02 to 0.20 at.% show a significant room temperature ferromagnetic response that is attributed to the formation of MnAs nanocrystals as confirmed from X-ray diffraction analysis and magnetization measurements. The influence of MnAs clusters on the formation of the nanostructures observed is discussed.

1. Introduction

The synthesis of semiconducting alloys presenting ferromagnetic behavior is of considerable current interest because it could be the basis for joining two large branches of Materials Science, semiconductors and ferromagnetic materials [1]. Potentially, this could give rise to the development of devices using both degrees of freedom, such as magnetic random-access memories, field-effect transistors, diodes or even solar cells [2–4]. For such applications, (Ga,Mn)As is one of the so-called diluted magnetic semiconductors (DMS) that has been subject of extensive attention in the last few years [5]. In spite of the low solubility of Mn into the GaAs matrix at the growth temperatures usually employed to grow GaAs epitaxial layers by Molecular Beam Epitaxy (MBE) (i.e., around 600 °C), by growing at low temperatures (below 300 °C) have been possible to fabricate (Ga,Mn)As with Mn concentration many times higher than its solubility limit [6]. Following this low temperature MBE method, (Ga,Mn)As samples presenting a Curie temperature (T_C) around 200 K has been achieved [7]. However, in spite of the considerable efforts carried out to optimize growth

parameters and post-growth thermal treatments it seems that a further increase in the T_C of (Ga,Mn)As is unlikely [7].

The formation of Mn-rich (Ga,Mn)As or MnAs nanoclusters integrated into the GaAs matrix have been also receiving increasing attention due to the observation of interesting room-temperature magneto-optical and magnetoresistance effects [8,9]. In fact, it has been reported that even at a low Mn content, Mn-rich (Ga,Mn)As nanoclusters embedded into the GaAs matrix synthesized by growing at low (250 °C) or moderate (350 °C) temperatures followed by a thermal annealing treatment at 500–650 °C, can exhibit a ferromagnetic response with a T_C as high as 360 K [9,10]. On the other hand, as semiconductor nanostructures possess important quantum effects and applications [11], the surfactant properties of Mn could be advantageous to self-assemble (Ga,Mn)As-based nanostructures presenting both, magnetic response and quantum confinement.

Early studies have been focused mainly on (Ga,Mn)As-based wire-shaped nanostructures. Nanowires were first obtained in layered (Ga,Mn)As structures produced by e-beam lithography [12]. First reports on the effect of catalytic properties of Mn in the growing of

* Corresponding authors at: Coordinación para la Innovación y Aplicación de la Ciencia y Tecnología (CIACyT), Universidad Autónoma de San Luis Potosí (UASLP), Av. Sierra Leona #550, Lomas 2a Sección, San Luis Potosí, S. L. P. 78210, Mexico (E. Cruz-Hernández).

E-mail addresses: risa008537@uaslp.mx (A. del Rio-de Santiago), esteban.cruz@uaslp.mx (E. Cruz-Hernández).

<https://doi.org/10.1016/j.jmmm.2018.12.030>

Received 2 August 2018; Received in revised form 30 November 2018; Accepted 9 December 2018

Available online 10 December 2018

0304-8853/ © 2018 Elsevier B.V. All rights reserved.